







ARTICLE

# Confinement hinders motility by inducing RhoA-mediated nuclear influx, volume expansion, and blebbing

Panagiotis Mistriotis<sup>1,2\*</sup> , Emily O. Wisniewski<sup>1,2\*</sup>, Kaustav Bera<sup>1,2</sup>, Jeremy Keys<sup>3</sup>, Yizeng Li<sup>2,4,5</sup>, Soontorn Tuntithavornwat<sup>1,2</sup>, Robert A. Law<sup>1,2</sup>, Nicolas A. Perez-Gonzalez<sup>1,2</sup>, Eda Erdogmus<sup>1</sup>, Yuqi Zhang<sup>1,2</sup>, Runchen Zhao<sup>1,2</sup> , Sean X. Sun<sup>2,4,6,7</sup> , Petr Kalab<sup>1,2</sup> , Jan Lammerding<sup>3</sup> , and Konstantinos Konstantopoulos<sup>1,2,4,6,8</sup> 

**Cells migrate in vivo through complex confining microenvironments, which induce significant nuclear deformation that may lead to nuclear blebbing and nuclear envelope rupture. While actomyosin contractility has been implicated in regulating nuclear envelope integrity, the exact mechanism remains unknown. Here, we argue that confinement-induced activation of RhoA/myosin-II contractility, coupled with LINC complex-dependent nuclear anchoring at the cell posterior, locally increases cytoplasmic pressure and promotes passive influx of cytoplasmic constituents into the nucleus without altering nuclear efflux. Elevated nuclear influx is accompanied by nuclear volume expansion, blebbing, and rupture, ultimately resulting in reduced cell motility. Moreover, inhibition of nuclear efflux is sufficient to increase nuclear volume and blebbing on two-dimensional surfaces, and acts synergistically with RhoA/myosin-II contractility to further augment blebbing in confinement. Cumulatively, confinement regulates nuclear size, nuclear integrity, and cell motility by perturbing nuclear flux homeostasis via a RhoA-dependent pathway.**

## Introduction

Cell migration through tissues is a critical step during the metastatic spread of cancerous cells from primary tumors to distal organs in the body. Metastasizing cells must travel through heterogeneous confining microenvironments in vivo that impose physical cues and initiate intracellular signaling cascades distinct from those experienced by cells during 2D migration (Paul et al., 2017; van Helvert et al., 2018). Specifically, pores in the ECM of tumor stroma and tunnel-like migration tracks are confining topographies that cells must navigate. These tunnel-like tracks may be generated by matrix remodeling of dense ECM by macrophages, cancer-associated fibroblasts, or leader cells, but pre-existing, 3D longitudinal tracks are also generated naturally by various anatomical structures (Paul et al., 2017). These paths impose varying degrees of confinement, as cells must travel through confining pores varying from 1 to 20  $\mu\text{m}$  in diameter, or fiber- and channel-like tracks ranging from 3 to 30  $\mu\text{m}$  in width and up to 600  $\mu\text{m}$  in length (Weigelin et al., 2012).

As the largest and stiffest cellular component (Lammerding, 2011), the nucleus has a rate-limiting role in cell migration through confined spaces (Davidson et al., 2014; Harada et al., 2014; Rowat et al., 2013; Wolf et al., 2013). In the absence of matrix degradation, tumor cell motility is halted at pore sizes smaller than  $\sim 7 \mu\text{m}^2$  due to lack of nuclear translocation (Wolf et al., 2013). Even at larger pore sizes, the nucleus poses a significant barrier to cell motility, and cells must transmit forces to the nucleus from the cytoskeleton in order to achieve efficient nuclear translocation (McGregor et al., 2016). One possible mechanism is through the linker of cytoskeleton and nucleoskeleton (LINC) complex, a network of SUN and nesprin proteins that mechanically connects the nucleus to the cytoskeleton (Crisp et al., 2006). Transmission of actomyosin contractile forces to the nucleus is essential for confined migration. When myosin contractility is inhibited, migration of cancer cells through collagen gels is significantly delayed due to insufficient

<sup>1</sup>Department of Chemical and Biomolecular Engineering, Johns Hopkins University, Baltimore, MD; <sup>2</sup>Johns Hopkins Institute for NanoBioTechnology, Johns Hopkins University, Baltimore, MD; <sup>3</sup>Meinig School of Biomedical Engineering and Weill Institute for Cell and Molecular Biology, Cornell University, Ithaca, NY; <sup>4</sup>Department of Mechanical Engineering, Johns Hopkins University, Baltimore, MD; <sup>5</sup>Department of Mechanical Engineering, Kennesaw State University, Marietta, GA; <sup>6</sup>Johns Hopkins Physical Sciences-Oncology Center, Johns Hopkins University, Baltimore, MD; <sup>7</sup>Department of Biomedical Engineering, Johns Hopkins University, Baltimore, MD; <sup>8</sup>Department of Oncology, Johns Hopkins University, Baltimore, MD.

\*P. Mistriotis and E.O. Wisniewski contributed equally to this paper; Correspondence to Konstantinos Konstantopoulos: [konstant@jhu.edu](mailto:konstant@jhu.edu).

© 2019 Mistriotis et al. This article is distributed under the terms of an Attribution–Noncommercial–Share Alike–No Mirror Sites license for the first six months after the publication date (see <http://www.rupress.org/terms/>). After six months it is available under a Creative Commons License (Attribution–Noncommercial–Share Alike 4.0 International license, as described at <https://creativecommons.org/licenses/by-nc-sa/4.0/>).

pushing forces at the cell rear (Thomas et al., 2015; Wolf et al., 2013). Additionally, actomyosin contractility, in conjunction with integrins and intermediate filaments, applies pulling forces to the nucleus from the cell leading edge (Petrie et al., 2014; Wolf et al., 2013).

Confinement exerts a mechanical stress on the nucleus, which can cause nuclear pressure buildup and ultimately lead to the blebbing and subsequent rupture of the nuclear envelope, resulting in DNA damage (Denais et al., 2016; Irianto et al., 2017; Raab et al., 2016). Compression of the nucleus by contractile actin fibers surrounding it causes spontaneous nuclear rupture events (Hatch and Hetzer, 2016; Takaki et al., 2017). However, nuclear rupture can occur in the absence of perinuclear actin simply upon mechanical compression of cells (Hatch and Hetzer, 2016). These findings suggest that compression of the nucleus, whether by actin fibers or external forces, is the main driver for nuclear envelope rupture. Consistent with these findings, nuclear rupture occurs at sites of high nuclear curvature (Xia et al., 2018). High actomyosin contractility, which increases cell and nuclear spreading (Buxboim et al., 2014, 2017), promotes nuclear rupture (Xia et al., 2018), while inhibition of actomyosin contractility results in more rounded nuclei with less frequent ruptures (Denais et al., 2016; Xia et al., 2018).

While several studies implicate actin and myosin in confinement-induced nuclear bleb formation and rupture (Denais et al., 2016; Hatch and Hetzer, 2016; Xia et al., 2018), it is unclear how contractile forces specifically promote this process. To address this question, we studied nuclear bleb formation by inducing cells to migrate via chemotaxis through collagen-coated microfluidic channels with fixed dimensions of 3  $\mu\text{m}$  in height, 10  $\mu\text{m}$  in width, and 200  $\mu\text{m}$  in length. In these confining channels, the nucleus acts as a plug, which compartmentalizes the cell posterior and anterior. We herein demonstrate that elevated and polarized RhoA/myosin-II activity induced by confinement, coupled with LINC complex-dependent anchoring of the nucleus at the cell posterior, locally increases cytoplasmic pressure and promotes passive influx of cytoplasmic constituents into the nucleus. In conjunction with deformation of the nucleus by perinuclear actomyosin bundles, this RhoA/myosin-II-dependent nuclear influx from the cell posterior promotes nuclear volume expansion, nuclear bleb formation, and subsequently nuclear envelope rupture.

## Results

### Confinement induces nuclear blebbing mediated by an actomyosin-dependent pathway involving the LINC complex

Using HT-1080 fibrosarcoma cells as a model, we observed that ~50–60% of cells migrating inside the physically constricted collagen-coated microchannels (width  $[W] \times$  height  $[H] = 10 \times 3 \mu\text{m}^2$ ) displayed nuclear blebs, which were identified as spherical-like bulges localized primarily at the leading edge of the nucleus (Fig. 1, a and b). Consistent with previous results (Denais et al., 2016), nuclear blebs were devoid of nuclear pore complexes (NPCs) but contained lamin-A (Fig. S1 a). In light of prior work showing that compression of cells between parallel plates is sufficient to induce nuclear bleb formation (Hatch and Hetzer, 2016; Le Berre et al., 2012), we fabricated wide ( $W = 50 \mu\text{m}$ ) microchannels with a

fixed height of 3  $\mu\text{m}$  to confine cells only in the apicobasal (i.e., top to bottom) direction. Although nuclear blebbing was observed in the 50- $\mu\text{m}$ -wide channels, it was significantly reduced compared with the 10- $\mu\text{m}$ -wide channels, which confine cells on all four sides (Fig. S1 b). Nuclear blebbing was the least frequent on unconfined, 2D surfaces (Fig. 1, a and b). These observations were reproduced using human osteosarcoma (HOS) cells (Fig. S1 c). In concert with recent findings (Denais et al., 2016; Raab et al., 2016), formation of nuclear blebs preceded or coincided with nuclear envelope rupture (Fig. 1 c). Nuclear rupture induced the rapid and reversible exchange of material between the nucleus and cytoplasm, as indicated by the use of two spectrally distinct reporters: one normally localized in the nucleus (NUP50-mCherry) and the other one in the cytoplasm (NLS-MBP-GFP-NES(Rev); Fig. 1 d and Fig. S1 d), and was more frequent in confinement than in 2D (Fig. 1 e). Of note, ~50% of cells with nuclear ruptures experienced multiple rupture/repair events at a rate of approximately one rupture per hour during migration through confined channels (Fig. S1, e–g). In contrast, we did not detect multiple rupture events within the observation period on unconfined 2D substrates (Fig. S1, e and f).

In light of prior work showing that both membrane bleb formation and nuclear envelope rupture require the activation of actomyosin contractility (Denais et al., 2016; Hatch and Hetzer, 2016; Sahai and Marshall, 2003), we hypothesized that formation of nuclear blebs also requires actomyosin contractility. In line with our hypothesis, inhibition of Rho-associated protein kinase (ROCK) or actomyosin contractility via cell treatment with Y27632 (10  $\mu\text{M}$ ; Fig. 1 f and Fig. S1 h) or blebbistatin (50  $\mu\text{M}$ ; Fig. S1 i), respectively, markedly suppressed nuclear blebbing in confinement, whereas expression of a constitutive active RhoA mutant (Q63L) increased nuclear blebbing (Fig. 1 f). Inhibition of ROCK correspondingly reduced nuclear rupture in confinement (Fig. S1 j). While individual knockdown of *myosin-IIA* (*MIIA* or *MYH9*) or *MIIIB* (*MYH10*; Fig. S1 k) had little effect on confinement-induced nuclear blebbing, dual silencing of *MIIA* and *MIIIB* repressed nuclear blebbing (Fig. 1 g). Myosin transmits forces to the nucleus via the LINC complex (Petrie et al., 2014). Thus, we next assessed the potential contributions of the LINC complex components SUN1 and SUN2 to nuclear blebbing in confinement. Silencing of *SUN1*, and to a lesser extent *SUN2* (Fig. S1 l), reduced nuclear blebbing in confinement (Fig. 1 h). To further verify the involvement of the LINC complex, we examined the effect of expression of EGFP-KASH2, which has been shown to act as a dominant-negative nesprin, causing mislocalization of endogenous nesprins and blocking force transmission to the nucleus (Lombardi et al., 2011; Stewart-Hutchinson et al., 2008), on nuclear blebbing. Compared with cells expressing a control EGFP-KASH2ext, EGFP-KASH2 cells had significantly reduced nuclear blebbing (Fig. S1 m). Together, these results demonstrate that myosin contractility via the LINC complex regulates nuclear bleb formation.

### Confinement induces RhoA activation, which triggers nuclear blebbing by promoting passive nuclear influx from the nuclear trailing edge

In light of the involvement of the RhoA/ROCK/myosin-II pathway in nuclear blebbing, we sought to determine the mechanism

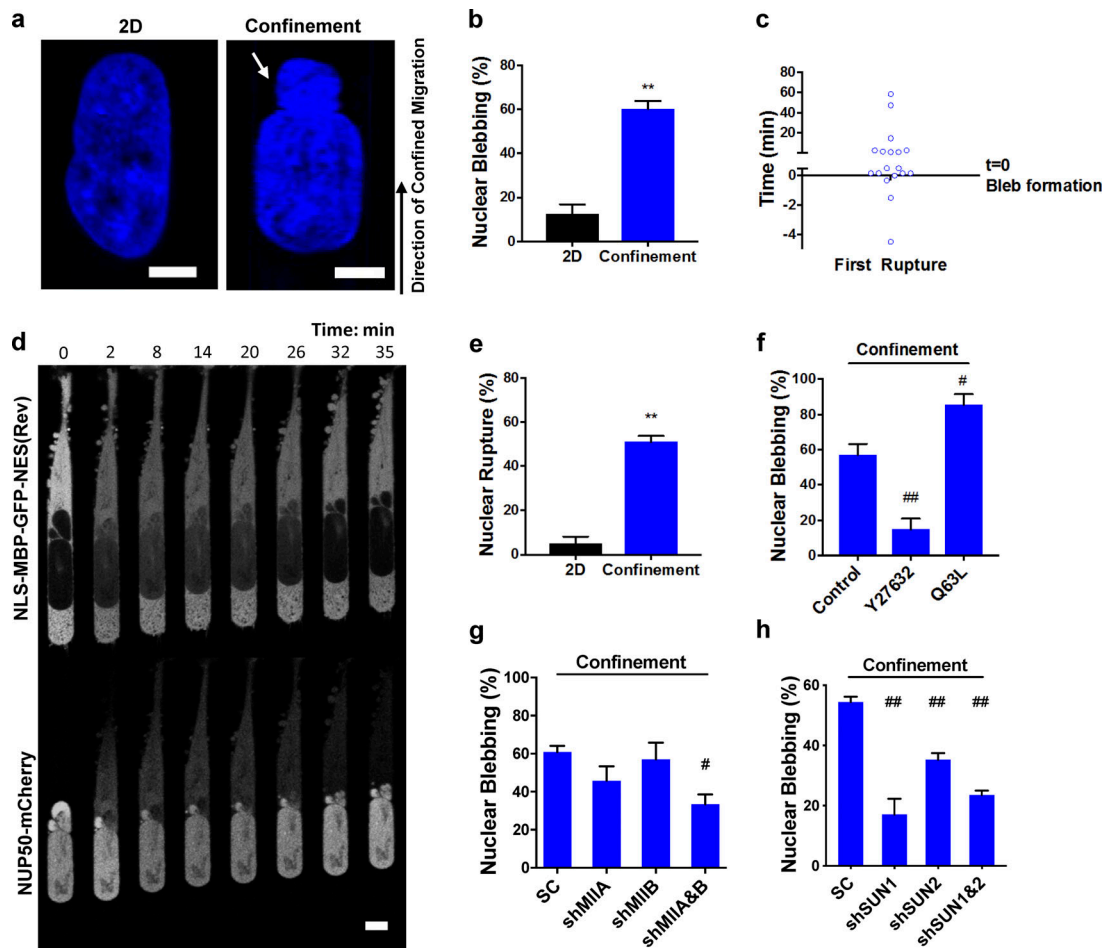


**Figure 1. Confinement promotes nuclear blebbing and rupture via a RhoA/ROCK/myosin-II/SUN1/2-dependent pathway.** (a) Representative images of the nucleus in 2D and confinement as visualized from cells fixed and stained with Hoechst. White arrow indicates nuclear bleb. Scale bars, 5  $\mu$ m. (b) Percentage of HT-1080 cells exhibiting nuclear blebbing in 2D versus confinement ( $n \geq 3$  independent experiments with a minimum of 30 cells per experiment). (c) Time required for the first incident of nuclear blebbing versus nuclear rupture as observed from HT-1080 cells expressing NLS-MBP-GFP-NES(Rev) or NUP50-mCherry ( $n = 3$  independent experiments with a minimum of five cells per experiment). (d) Image sequence of an HT-1080 cell experiencing transient nuclear rupture in confined channels visualized by NLS-MBP-GFP-NES(Rev) mislocalization in the nucleus and NUP50-mCherry mislocalization in the cytoplasm. Scale bar, 10  $\mu$ m. (e) Percentage of HT-1080 cells experiencing nuclear rupture in 2D and confinement, as quantified from mislocalization of NLS-MBP-GFP-NES(Rev) from the cytoplasm to the nucleus ( $n = 4$  independent experiments with a minimum of eight cells per experiment). (f) Percentage of control, 10  $\mu$ M Y27632-treated, and constitutively active RhoA (Q63L) HT-1080 cells displaying nuclear blebbing, as observed from cells fixed and stained with Hoechst ( $n \geq 3$  independent experiments with a minimum of 15 cells per experiment). (g) Percentage of scramble control, MIIA-knockdown, MIIB-knockdown, and dual MIIA/B-knockdown HT-1080 cells displaying nuclear blebbing, as observed from cells fixed and stained with Hoechst ( $n \geq 3$  independent experiments with a minimum of 15 cells per experiment). (h) Percentage of scramble control, SUN1-knockdown, and/or SUN2-knockdown HT-1080 cells displaying nuclear blebbing ( $n \geq 3$  independent experiments with a minimum of 15 cells per experiment). Values represent mean  $\pm$  SEM. \*\*,  $P < 0.01$  relative to 2D; #,  $P < 0.05$ ; ##,  $P < 0.01$  relative to confined control or scramble control (SC).

by which these molecules promote nuclear bleb formation in confinement. To explore this, we first quantified RhoA activity of cells in 2D versus confinement using a Förster resonance energy transfer (FRET)-based RhoA activity biosensor (Fritz et al., 2013). Using this biosensor, RhoA activation is detected by increased FRET in the closed conformation, in which the GTP-loaded RhoA domain interacts with the rhotekin Rho-binding domain, bringing the mTFP-1 (cyan) donor and YFP acceptor closer to each other. To verify that this sensor works as expected, we showed that treatment of HT-1080 cells plated on a 2D unconfined surface with Rho activators, such as FBS, the catalytic domain of bacterial cytotoxic necrotizing factor (CNF) toxins, and lysophosphatidic acid, significantly increased the

wide-field FRET emission intensity ratio (ratio of the acceptor emission upon donor excitation over donor emission; Fig. S2, a–c). Conversely, treatment with the Rho inhibitor C3 transferase significantly decreased the wide-field FRET emission intensity ratio (Fig. S2 d). Moreover, the FRET ratio did not change when an empty FRET linker was used (Fig. S2 e). These results were also validated using confocal fluorescence-lifetime imaging microscopy (FLIM), which measures increases in FRET efficiency of the RhoA sensor through decreased donor fluorescence lifetime (Fig. S2, f and g). FLIM measurements revealed that cells in confinement exhibited overall higher levels of RhoA activity than cells in 2D (Fig. 2 a). Importantly, confined cells displayed spatial regulation of RhoA, with maximal activity

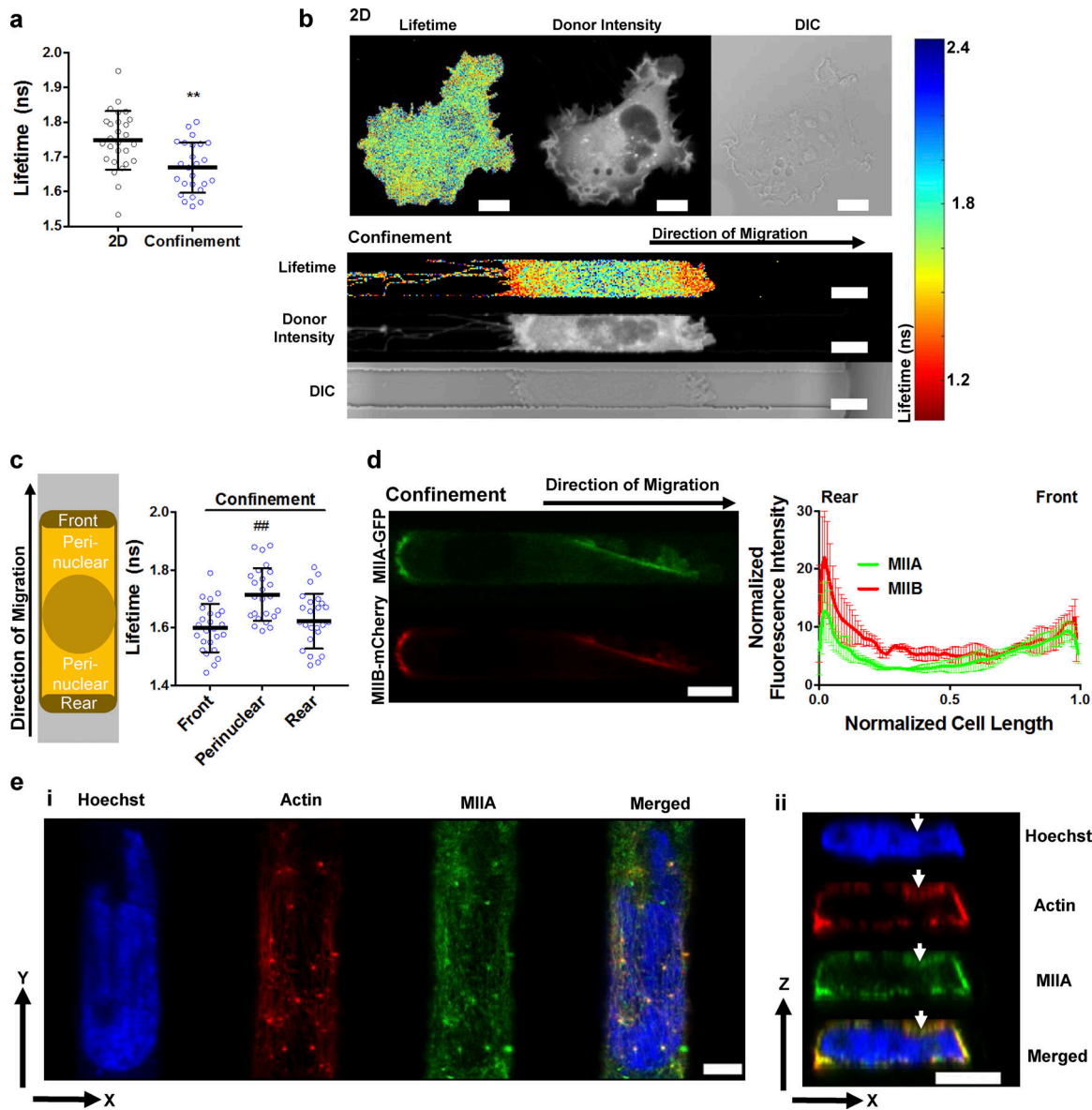


**Figure 2. Confinement spatially regulates RhoA/myosin-II dependent contractility.** (a) Donor fluorescence lifetime of RhoA activity biosensor on 2D and in confinement, as measured by FLIM-FRET ( $n \geq 25$  cells from three independent experiments). (b) Heat map of RhoA activity biosensor in representative cells on 2D or in confinement, as imaged by FLIM-FRET (scale bars, 10  $\mu\text{m}$ ). DIC, differential interference contrast. (c) Schematic (left) depicting the front, perinuclear, and rear cell regions and spatial distribution of RhoA activity inside confined microchannels (right) as measured by FLIM-FRET ( $n \geq 25$  cells from three independent experiments). (d) Representative image (left) and quantification (right) of the average intensity of MIIA and MIIB across the cell length of confined cells, as visualized by MIIA-GFP and MIIB-mCherry (quantification from 16 cells). Scale bar, 10  $\mu\text{m}$ . (e) Super-resolution images of the perinuclear actin and myosin-IIA of a representative HT-1080 cell (out of 10 cells analyzed) expressing myosin-IIA-GFP and stained for actin phalloidin (red) and Hoechst (blue) inside a confined channel. (i) XY plane, apical surface; (ii) orthogonal view, XZ plane. Arrows indicate regions of nuclear deformation. Scale bars, 5  $\mu\text{m}$ . Data represent the mean  $\pm$  SD. \*\*,  $P < 0.01$  relative to 2D; ##,  $P < 0.01$  relative to confined front/rear.

observed at the cell poles (Fig. 2, b and c). In contrast, 2D cells had relatively uniform RhoA activity (Fig. 2 b).

In light of the distinct localization of RhoA activity exhibited in confined cells as well as the role of myosin-II in nuclear bleb formation, we examined myosin-II localization in cells in confinement. First, we examined MIIA and MIIB isoforms to determine if they displayed a similar polarization pattern to RhoA activity. Interestingly, MIIA and MIIB showed the highest localization at the cell rear in  $\sim 70\%$  of migrating cells (Fig. 2 d). We also examined myosin-II localization around the nucleus. Using

super-resolution imaging, we observed distinct MIIA fibers on the apical surface of the nucleus of confined cells (Fig. 2 e). These myosin-II fibers colocalized with actin and strongly accumulated in regions of nuclear deformation, suggesting that these actomyosin bundles deformed the nucleus nonuniformly on its apical surface.

In light of this RhoA/myosin-II polarization in confinement, we hypothesized that elevated actomyosin contractility at the cell rear locally increases cytoplasmic pressure. Because the nucleus separates the posterior and anterior poles of cells in



confining channels (Fig. S3 a), the equilibration of differential cytoplasmic pressure throughout the cell could result in fluid flux into the nucleus. In conjunction with increased intranuclear pressure resulting from direct actomyosin compression of the nucleus (Fig. 2 e), this influx of cytoplasmic constituents into the nucleus could ultimately pressurize the nucleus, promoting nuclear blebbing and rupture. Cytoplasmic pressure-driven nuclear intake, which we define as passive nuclear influx, would be feasible for molecules smaller than the estimated size exclusion limit of NPCs (~40–60 kD; Stewart, 2007). To test this hypothesis, we transfected HT-1080 cells with a photo-activatable GFP construct (PA-GFP), which has a low molecular mass (~25 kD), is distributed throughout the cell, and becomes fluorescent only upon UV-light illumination. By locally activating PA-GFP either in the posterior or anterior cytoplasmic compartment (Fig. 3 a), we monitored PA-GFP entry into the nucleus and calculated the half-time ( $t_{1/2}$ ) of nuclear influx. Confinement induced increased passive nuclear influx selectively from the posterior compartment, as evidenced by lower  $t_{1/2}$  compared with those for the anterior compartment and cells on unconfined 2D surfaces (Fig. 3 b). This was also observed in HOS cells (Fig. S3 b). By activating PA-GFP inside the nucleus and tracking the decay of its signal intensity, we determined that passive nuclear efflux remained unaffected for cells in confinement relative to 2D (Fig. S3 c).

Interestingly, cells inside wider channels ( $W \times H = 50 \times 3 \mu\text{m}^2$ ) displayed reduced passive nuclear influx from the posterior compared with tightly confined ( $W \times H = 10 \times 3 \mu\text{m}^2$ ) cells (Fig. 3 c). This difference can be explained by the fact that in wider microchannels, the pressure differential is alleviated since the nucleus does not fully occlude the channels' cross-sectional area (Fig. S3 a) and thus pressure can be equilibrated through gaps between the nucleus and side walls of the microchannels. In contrast, in tightly confined cells, the nucleus acts as a plug, which compartmentalizes the cell posterior and anterior (Fig. S3 a), thereby facilitating pressure buildup at the cell rear. This is further corroborated by data showing that upon PA-GFP activation at the cell cytoplasmic trailing edge, a pronounced delay in flow to the cell leading edge was observed in tightly confined cells but not in wider ( $W = 50 \mu\text{m}$ ) microchannels or on 2D (Fig. S3 d). The population of tightly confined ( $W \times H = 10 \times 3 \mu\text{m}^2$ ) cells included both nuclear bleb-bearing and nuclear bleb-free cells. We thus speculated that the effects of nuclear compartmentalization and pressure buildup at the cell rear might be exacerbated in the nuclear bleb-bearing population. Indeed, cytoplasmic flow from the cell trailing to leading edge was significantly decreased for nuclear bleb-bearing as compared with nuclear bleb-free cells (Fig. S3 e), presumably because the gaps between the nucleus and the side walls of the microchannels were narrower in these cells. Importantly,  $t_{1/2}$  of cytoplasmic flow and nuclear influx were comparable for bleb-bearing cells (Fig. S3 e). In distinct contrast, cytoplasmic flow was significantly faster than nuclear influx in bleb-free cells (Fig. S3 e), suggesting that pressure in this case could be equilibrated through the cytoplasm, thereby preventing nuclear blebbing. These data further support the notion that the nucleus can separate the posterior and anterior cell compartments in fully

confined spaces, as has been shown previously (Petrie et al., 2014), and demonstrate the importance of an intracellular pressure gradient, maintained by this nuclear occlusion of the cell, in promoting nuclear influx and bleb formation.

To distinguish the roles of pressure-driven convection versus diffusion of PA-GFP in nuclear influx, we applied either a hypotonic (165 mOsm) or hypertonic (620 mOsm) shock at the cell leading or trailing edge, respectively (Fig. 3, d and e). Exposure to a hypotonic shock at the cell front, which drives water influx and consequently pressure buildup in the cell front compartment, increased PA-GFP nuclear influx from the cell anterior (Fig. 3 d). On the other hand, exposure to a hypertonic shock at the cell rear, which has the exact opposite effect on the cell rear compartment, decreased PA-GFP nuclear influx from the cell posterior (Fig. 3 e). To provide further evidence for the presence of pressure-driven fluid convection, we activated PA-GFP inside the nucleus of confined cells and measured the flow of PA-GFP from the rear to the front of the nucleus and vice versa. PA-GFP flow from the rear to the front of the nucleus was significantly faster than flow in the opposite direction (Fig. S3 f). Collectively, these experiments reveal that convection of fluid due to pressure buildup at the cell posterior leads to elevated nuclear influx during confined migration.

Nuclear influx, but not efflux, increased in bleb-bearing but not bleb-free nuclei (Fig. 3 f and Fig. S3 g), suggesting that actomyosin contractility is required for increased passive nuclear influx. Indeed, ROCK inhibition suppressed passive nuclear influx through the trailing nuclear edge in confined cells (Fig. 3 f). To verify that actomyosin contractility promotes nuclear influx and bleb formation by increasing cytoplasmic pressure and thus forcing cytoplasmic constituents into the nucleus, we measured nuclear influx after laser ablation of the actomyosin cortex at the cell's trailing edge (Fig. 3, g and h). Upon laser ablation of the actomyosin cortex, a large pressure-driven membrane bleb formed in the ablated region (Fig. 3 h), thereby allowing relaxation of internal cytoplasmic pressure as previously reported (Tinevez et al., 2009). Importantly, diffuse cytoplasmic GFP stayed within the cytoplasm after ablation, indicating that laser ablation disrupted only the cortical actomyosin network while leaving the plasma membrane intact (Fig. 3 h and Fig. S3 h). In line with our hypothesis, nuclear influx was significantly decreased in laser-ablated cells compared with control cells (Fig. 3 g).

In light of prior work showing that the LINC complex is important for controlling nuclear position in cells migrating through 3D matrices by directly tethering the nucleus to the cytoskeleton (Petrie et al., 2014), we hypothesized that in confined microchannels, elevated pressure at the cell posterior would push the nucleus toward the leading edge of the cell in the absence of the LINC complex. This forward movement of the nucleus would thus alleviate pressure in the cell's posterior compartment, thereby reducing influx. In agreement with this hypothesis, the nucleus was indeed located closer to the front of the cell when SUN1 was depleted (Fig. 3 i). Moreover, SUN1 knockdown reduced nuclear influx of confined cells (Fig. 3 j), whereas nuclear influx of unconfined cells was unaffected by SUN1 depletion (Fig. S3 i). Collectively, these data suggest that

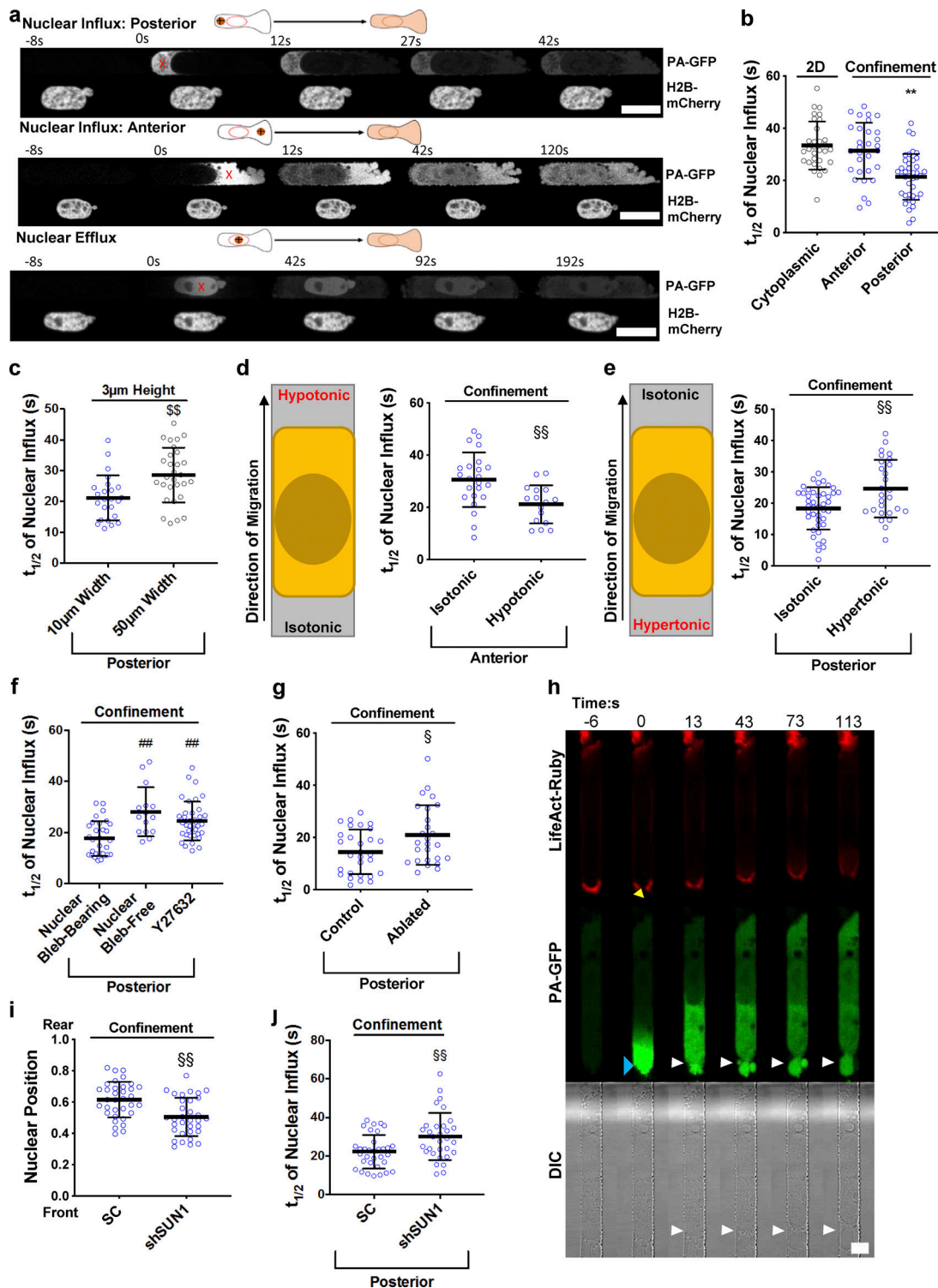


**Figure 3. Confinement induces elevated nuclear influx that correlates with nuclear blebbing.** (a) Time-dependent image sequence of PA-GFP influx into the nucleus from the posterior (top image sequence) or anterior (middle image sequence) compartment, or efflux from the nucleus (bottom image sequence) upon UV excitation in confinement. Red "X" symbols represent points of excitation. Scale bars, 20  $\mu$ m. (b) Quantification of transport of PA-GFP into the nucleus of HT-1080 cells on 2D or inside confined channels following UV illumination in the anterior or posterior compartments, reported as the  $t_{1/2}$  required for the signal (PA-GFP) to reach maximum intensity in the nucleus ( $n \geq 27$  cells from three or more independent experiments). (c)  $t_{1/2}$  of PA-GFP nuclear influx from the cell posterior for HT-1080 cells inside 10- $\mu$ m- and 50- $\mu$ m-wide channels with a fixed height of 3  $\mu$ m ( $n \geq 24$  cells from three independent experiments). (d) Schematic (left) and quantification (right) of  $t_{1/2}$  of PA-GFP nuclear influx for confined HT-1080 cells exposed to a hypotonic shock (165 mOsm) at their leading edge ( $n \geq 16$  cells from three independent experiments). (e) Schematic (left) and quantification (right) of  $t_{1/2}$  of PA-GFP nuclear influx for confined HT-1080 cells exposed to a hypertonic shock (620 mOsm) at their trailing edge ( $n \geq 27$  cells from five independent experiments). (f)  $t_{1/2}$  of PA-GFP nuclear influx for confined cells with and without nuclear blebs, as well as Y27632-treated (10  $\mu$ M) HT-1080 cells ( $n \geq 15$  cells from four or more independent

experiments). **(g)**  $t_{1/2}$  of PA-GFP nuclear influx for control versus actin cortex-ablated HT-1080 cells. Simultaneous photoablation and photoactivation occurred at the cell trailing edge ( $n \geq 26$  cells from four independent experiments). **(h)** Time-dependent image sequence of simultaneous actin cortex ablation (top) and PA-GFP influx into the nucleus (bottom) at the cell posterior. Yellow arrow indicates ablation. Blue arrow indicates photoactivation. White arrows indicate bleb formation as a result of ablation. Scale bar, 10  $\mu\text{m}$ . **(i)** Nuclear position of scramble control versus SUN1-KD HT-1080 cells ( $n \geq 33$  cells from three independent experiments). **(j)**  $t_{1/2}$  of PA-GFP nuclear influx for confined scramble control cells and SUN1-knockdown HT-1080 cells ( $n \geq 31$  cells from three independent experiments). Values represent mean  $\pm$  SD. \*\*,  $P < 0.01$  relative to 2D cytoplasmic, confinement anterior; \$\$,  $P < 0.01$  relative to 10  $\mu\text{m}$  width; ##,  $P < 0.01$  relative to confinement nuclear bleb-bearing; §,  $P < 0.05$ ; §§,  $P < 0.01$  relative to scramble/isotonic/control.

the LINC complex tethers the nucleus closer to the cell rear, which, in conjunction with the pressure buildup at the cell posterior due to elevated RhoA/myosin-II activity, facilitates nuclear influx.

### Disruption of nuclear flux homeostasis alters nuclear blebbing

Under isotonic conditions, nuclear blebs formed almost exclusively on the front side of the nucleus (Fig. 4 a), likely due to increased nuclear influx from the cell posterior. If this were true, then elevation of nuclear influx from the cell anterior should lead to the formation of nuclear blebs at its trailing edge. To test this hypothesis, we exposed cells to a hypotonic shock at their leading edge (165 mOsm or 85.5 mOsm), which should cause water influx into the cell and concomitant pressure buildup at the cell anterior. Indeed, this intervention significantly increased nuclear blebbing on the rear side of the nucleus in an osmolarity-dependent manner (Fig. 4 a), demonstrating that elevated cytoplasmic pressure promotes nuclear influx, which results in nuclear bleb formation.

Because elevated nuclear influx resulted in nuclear blebbing, we hypothesized that perturbation of nuclear flux homeostasis would alter the frequency of nuclear blebbing. We treated cells

with the exportin-1 inhibitor Leptomycin B (LMB), which disrupts active nuclear export. We speculated that, as a consequence of nuclear export inhibition, nuclear export signal (NES) cargo accumulation in the nucleus (Kudo et al., 1999; Wolff et al., 1997) would lead to increased nuclear viscosity, and consequently slower transport, thereby also indirectly slowing down passive nuclear efflux. To verify this, we quantified the transport of PA-GFP within the nuclear compartment of control and LMB-treated cells as a measure of nuclear viscosity. Transport of PA-GFP inside the nucleus was significantly slower in LMB-treated as compared with vehicle control (VC) cells, supporting this model (Fig. S4 a). Cell treatment with a LMB concentration (20 nM), which is frequently used in the literature (Vartiainen et al., 2007), suppressed both active nuclear export of the cytoplasmic reporter NLS-MBP-GFP-NES(Rev) on 2D surfaces (Fig. S4 b) and passive macromolecule exit from the nucleus (Fig. 4 b), while passive nuclear influx was only modestly reduced (Fig. S4 c). This concentration of LMB increased nuclear blebbing of cells on 2D (Fig. 4 c), suggesting that inhibition of nuclear efflux is sufficient to increase nuclear blebbing. Moreover, LMB further increased nuclear blebbing in confinement (Fig. 4 c). Interestingly, even in the presence of the ROCK

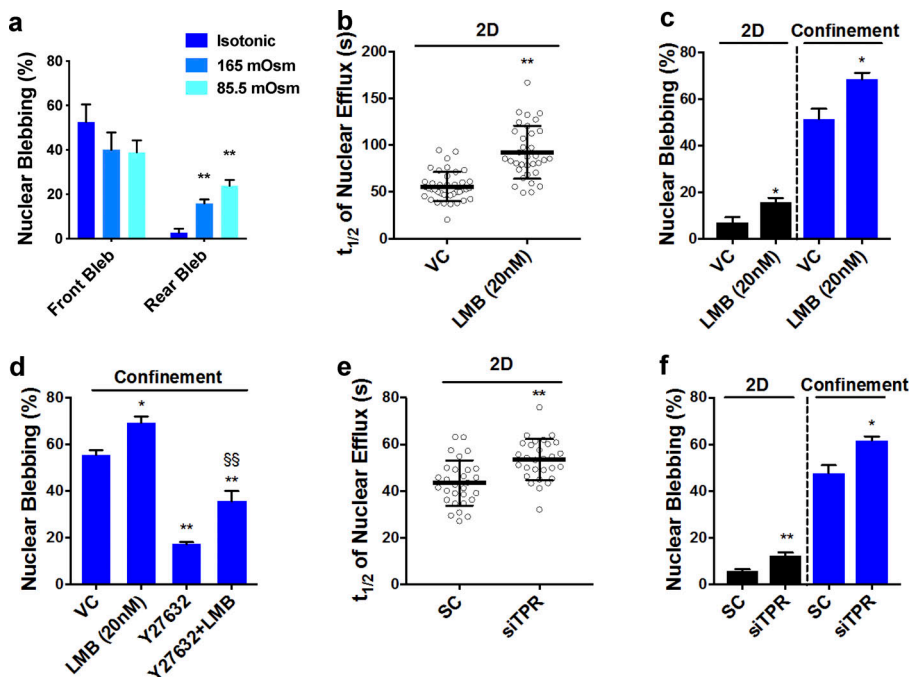


**Figure 4. Perturbation of passive nuclear transport dynamics alters nuclear bleb formation.** **(a)** Percentage of HT-1080 cells displaying nuclear blebbing on the front or rear of the nucleus after being exposed to a hypotonic shock (165 or 85.5 mOsm) at their leading edge ( $n \geq 3$  independent experiments with a minimum of 20 cells per experiment). **(b)**  $t_{1/2}$  of PA-GFP signal diffusing from the nucleus to the cytoplasm of VC or LMB-treated (20 nM) HT-1080 cells plated on 2D ( $n \geq 29$  cells from three or more independent experiments). **(c)** Percentage of VC and LMB-treated (20 nM) HT-1080 cells in confinement and on 2D displaying nuclear blebbing, as observed from cells fixed and stained with Hoechst ( $n \geq 3$  independent experiments with a minimum of 20 cells per experiment). **(d)** Percentage of cells displaying nuclear blebs after treatment with vehicle, Y27632, LMB, or Y27632 and LMB ( $n \geq 5$  independent experiments with a minimum of 14 cells per experiment). **(e)**  $t_{1/2}$  of PA-GFP signal diffusing from the nucleus to the cytoplasm of scramble control or TPR-knockdown HT-1080 cells plated on 2D ( $n \geq 29$  cells from three or more independent experiments). **(f)** Percentage of scramble control and TPR-knockdown HT-

1080 cells in confinement and on 2D displaying nuclear blebbing, as observed from cells fixed and stained with Hoechst ( $n \geq 3$  independent experiments with a minimum of 20 cells per experiment). Values represent mean  $\pm$  SD (b and e) or mean  $\pm$  SEM (a, c, d, and f). \*,  $P < 0.05$ ; \*\*,  $P < 0.01$  relative to vehicle/scramble control or isotonic rear bleb; §§,  $P < 0.01$  relative to Y27632.

pathway inhibitor Y27632 (Fig. 4 d), LMB-treated cells exhibited elevated nuclear blebbing as compared with cells treated with Y27632 alone. These data reveal that inhibition of nuclear efflux can act synergistically with RhoA/myosin-II contractility to further augment blebbing.

We wished to verify the effects of LMB on nuclear efflux and blebbing were not caused by potential off-target effects of the drug. Previous studies have indicated that the nuclear pore basket protein TPR (translocated promoter region) has an important role in nuclear export (Bangs et al., 1998; Frosst et al., 2002) in a manner that involves TPR interaction with exportin 1–cargo complexes (Ben-Efraim et al., 2009). Although TPR is also required for nuclear import of large cargos (Snow et al., 2013) and unspliced mRNAs (Rajanala and Nandicoori, 2012), inhibition of TPR induced strong nuclear accumulation of nuclear export cargos without affecting the import of smaller cargos (Frosst et al., 2002). Therefore, we hypothesized that the RNAi-mediated depletion of TPR would mimic the effects of LMB. Indeed, siRNA silencing of TPR (Fig. S4 d) significantly delayed passive nuclear efflux (Fig. 4 e) and to a lesser extent influx (Fig. S4 e), thereby resulting in increased nuclear blebbing both on 2D surfaces and in confinement (Fig. 4 f). Taken together, these data reveal that deregulation of the homeostatic balance of nuclear influx and efflux (influx > efflux) is sufficient to promote nuclear blebbing.

#### Elevated nuclear influx promotes nuclear volume expansion and decreases cell motility

Due to the increased nuclear influx observed in bleb-bearing cells, we hypothesized that the formation of nuclear blebs would coincide with an increase in nuclear size. To demonstrate this, we examined changes in nuclear longitudinal areas and nuclear volumes for bleb-bearing and bleb-free cells. For bleb-bearing cells, several rupture/repair events were detected during cell migration in confinement (Fig. 5, a and b). Upon nuclear rupture, the bleb size (Fig. 5 a) and the total longitudinal area of the nuclear bleb and body decreased instantly (Fig. 5 b), consistent with previous observations (Denais et al., 2016). Bleb size and nuclear longitudinal area both increased gradually following nuclear envelope repair until the next rupture event. Nuclear longitudinal area was larger in nuclear bleb-bearing than bleb-free cells in confinement (Fig. S5 a) and correlated with the overall area of nuclear blebs (Fig. S5 b). Importantly, for these confined cells, the nuclear volume always occupied the entire height (Z-direction) of the channel, suggesting that the increased nuclear longitudinal area (XY projection) of nuclear bleb-bearing cells was indicative of increased nuclear volume. Indeed, bleb-bearing cells had significantly larger volumes than bleb-free cells, as measured from confocal 3D image reconstructions (Fig. 5 c). Moreover, the nuclear volumes of all bleb-bearing cells increased with time in confinement, whereas only ~30% of bleb-free cells displayed moderately increased nuclear volumes over time (Fig. 5 d and Fig. S5 c). Bleb-free cells whose nuclear volume increased tended to have a longer duration of migration in confinement (Fig. S5 c). Interestingly, nuclear blebs grew to an average of ~2.8 times their initial size during migration in confinement, while only a mild, yet

consistent, volume increase was observed in the nuclear body (Fig. 5 e). The confinement-induced nuclear volume expansion on the order of ~15% detected in this work is in line with findings from other microfluidic systems after cell exit from a highly confining environment (Davidson et al., 2015). Roughly half of this volume increase stemmed from nuclear body volume expansion and the remaining half from the growing nuclear bleb size (Fig. 5 f). ROCK inhibition, which suppressed nuclear blebbing, also reduced nuclear volume (Fig. 5 g) and nuclear longitudinal area (Fig. S5, d and e) in confinement. In contrast, constitutive activation of RhoA increased nuclear volume (Fig. 5 g). Because actomyosin contractile forces are transmitted from the cytoskeleton to the nucleus via the LINC complex, depletion of the LINC complex components SUN1 and 2, which inhibited nuclear blebbing, also reduced nuclear longitudinal area (Fig. S5 f). Conversely, treatment with LMB delayed nuclear efflux and increased nuclear blebbing (Fig. 4, a and b), so we investigated whether this intervention also affected nuclear volume. Indeed, LMB treatment increased the nuclear volume of cells seeded on both 2D surfaces (Fig. 5 h) and inside confined microchannels (Fig. 5 i).

We next explored the effect of nuclear size increase on the cells' migratory potential. Changes in nuclear volume affect the size of the perinuclear space between the nucleus and the channel wall, which subsequently modulates the pattern of cytosolic flow through this perinuclear space. Therefore, we modeled the fluid dynamics within the perinuclear space based on lubrication theory (Kundu et al., 2011) to predict the effect of nuclear volume changes on cell migration speed. This mathematical model predicted that below a nuclear volume threshold, nuclear size would vary inversely with migration speed in confinement (Fig. 5 j). Above this threshold, cell speed would reach a minimum and remain unaltered upon further increasing nuclear size (Fig. 5 j). The initial linear decrease in cell speed is dictated by the dominant effect of nuclear volume increase in the lateral and vertical directions, which shrinks the perinuclear space and increases friction between the nucleus and the channel wall. Once expansion in the lateral and vertical directions is maximized, further nuclear expansion occurs at the front and rear of the nucleus, which has no effect on the perinuclear space and therefore results in a plateau in migration speed. To verify the predictions of this model, we examined the relationship between nuclear size and cell speed in confinement, using nuclear longitudinal area as a proxy for nuclear volume (Fig. 5 k). In line with our mathematical model, increased nuclear longitudinal area correlated with decreased migration speed until the nuclear area reached ~350  $\mu\text{m}^2$  (Fig. 5 k). After this point, nuclear size had no further effect on cell speed (Fig. 5 k). Collectively, these results demonstrate that confined migration can promote nuclear volume expansion, which has negative effects on cells' migratory potential.

## Discussion

Nuclear envelope blebbing and rupture represent deleterious consequences of confined cell migration, and may have potentially detrimental effects on genomic stability (Denais et al.,



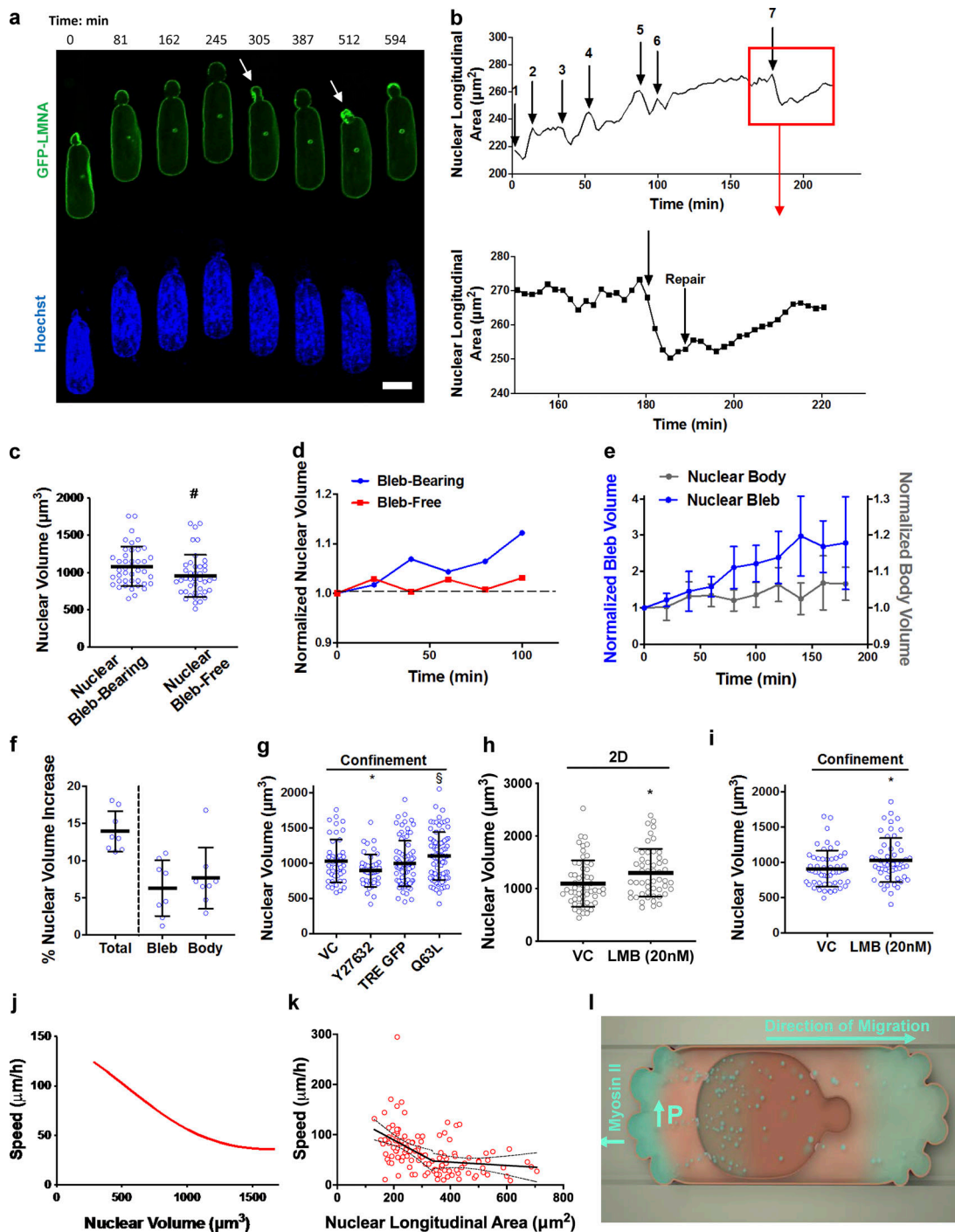


**Figure 5. Nuclear bleb formation corresponds to nuclear volume expansion and decreased migration speed.** (a) Image sequence depicting the growth and subsequent collapse of the nuclear envelope of HT-1080 cells during nuclear blebbing and rupture in confinement. Arrows indicate time frame of rupture events. Scale bar, 10  $\mu\text{m}$ . (b) Time-dependent change of nuclear longitudinal area of an H2B-mCherry labeled HT-1080 cell during migration in confinement. Arrows indicate incidents of nuclear rupture (top). Time-dependent change of nuclear longitudinal area of an H2B-mCherry labeled HT-1080 cell over the course of one nuclear rupture and repair (bottom). (c) Nuclear volume, measured from confocal Z-stacks of HT-1080 H2B-mCherry nuclear bleb-bearing and nuclear bleb-free cells in confinement ( $n \geq 42$  cells from four independent experiments). (d) Change in nuclear volume over time of migration through confined channels for representative bleb-bearing and bleb-free cell, as measured from confocal Z-stacks of HT-1080 H2B-mCherry cells. (e) Change in volume over time of migration through confined channels of the nuclear bodies and nuclear blebs, as measured from confocal Z-stacks of HT-1080 H2B-mCherry cells ( $n = 9$  cells from two independent experiments). (f) Percentage of nuclear volume increase relative to the total initial nuclear volume for the total nucleus, nuclear bleb, and nuclear body ( $n = 8$  cells from two independent experiments). (g) Nuclear volume, measured from confocal Z-stacks of HT-1080 H2B-mCherry control and Y27632-treated cells and TRE GFP control and Q63L infected cells in confinement ( $n \geq 50$  cells from three or more independent experiments). (h) Nuclear volume, measured from confocal Z-stacks of HT-1080 H2B-mCherry control and LMB-treated cells on 2D ( $n \geq 52$  cells from 3 independent experiments). (i) Nuclear volume, measured from confocal Z-stacks of HT-1080 H2B-mCherry control and LMB-treated cells in confinement ( $n \geq 53$  cells from three independent

experiments). **(j)** Cell migration speed as a function of nuclear volume as predicted by mathematical modeling based on lubrication theory. **(k)** HT-1080 speed plotted as a function of nuclear longitudinal area ( $n = 120$  cells from four independent experiments). Solid line represents the best fit, and dotted lines represent the 95% CI. **(l)** Schematic describing the proposed mechanism for nuclear bleb formation. P denotes pressure. \*,  $P < 0.05$  relative to vehicle/scramble control; #,  $P < 0.05$  relative to nuclear bleb bearing; §,  $P < 0.05$  relative to TRE GFP control. Scale bar, 10  $\mu\text{m}$ .

2016; Irianto et al., 2017; Raab et al., 2016). We herein propose a model by which confinement activates RhoA triggering myosin-II-dependent cortical contractility (Amano et al., 1996) at the cell trailing edge. In light of the direct link between contractility and intracellular pressure (Petrie et al., 2014; Sao et al., 2019), we postulate that elevated contractility along with the preferential tethering of the nucleus toward the cell rear locally increases cytoplasmic pressure in the posterior compartment of the cell, thereby promoting passive nuclear influx through the channels of NPCs. Elevated nuclear influx consequently pressurizes the nucleus, leading to nuclear volume expansion, nuclear envelope blebbing, and rupture (Fig. 5 l). Confinement may also promote nuclear import by directly stretching NPCs and exposing their cytosolic side during nuclear flattening, as recently demonstrated for cells on stiff substrates (Elosegui-Artola et al., 2017). However, NPC stretching may also result in increased passive nuclear efflux, which we did not observe in our study. This suggests that myosin-II-dependent buildup of cytoplasmic pressure at the cell posterior is the main driving force for increased nuclear influx. Although pressure was not measured directly in our experiments, several lines of evidence point to a role of posterior cytoplasmic pressure in promoting nuclear influx. Laser ablation of the actomyosin cortex at the cell trailing edge, which has previously been shown to relax cytoplasmic pressure (Tinevez et al., 2009), as well as exposure of the cell trailing edge to a hypertonic shock, which drives water out of the cell, both significantly reduce nuclear influx from the cell posterior. On the other hand, exposure of the cell leading edge to a hypotonic shock significantly increases nuclear influx from the cell anterior. Furthermore, measurements of PA-GFP flow within the nucleus reveal that flow from the rear to the front of the nucleus is significantly faster than flow in the opposite direction. Collectively, these experiments point to the existence of a pressure gradient in tightly confined cells. In the case of nuclear bleb-free cells, cytoplasmic flow around the nucleus is markedly faster than nuclear influx and, as such, pressure is primarily equilibrated through the cytoplasm, thereby preventing nuclear blebbing. In contrast, the  $t_{1/2}$  of cytoplasmic flow and nuclear influx are comparable for bleb-bearing cells, suggesting that pressure equilibration must occur through the nucleus and contribute to nuclear blebbing. Taken together, our work suggests that a cytoplasmic pressure gradient is critical for elevated nuclear influx and nuclear bleb formation.

While our work implicates myosin-II-dependent cytoplasmic pressure at the cell posterior in nuclear bleb formation in confinement, previous studies have demonstrated that myosin-II and vimentin transmit a pulling force to the nucleus after binding with nesprin3 and pressurize the cell anterior during migration through 3D environments (Petrie et al., 2014). Although we cannot distinguish between nuclear pulling versus pushing, our data using PA-GFP reveal elevated nuclear influx

rates at the trailing, but not the leading, edge of confined cells, thus suggesting a dominant role for pushing over pulling forces in our microfluidic system. Consistent with this, MIIA and MIIB are primarily enriched at the trailing edge of confined cells (Thomas et al., 2015). However, given cells' migration plasticity (Petrie and Yamada, 2016), it is likely that cells can switch between myosin-II-mediated pushing and pulling mechanisms in response to the distinct physical cues of the extracellular microenvironment, such as longitudinal migration tracks versus dense ECM, in order to translocate their nucleus most efficiently. Additionally, the mode of migration may dictate whether pulling versus pushing forces dominate. For instance, while cells migrating with a lobopodial phenotype have been shown to primarily exert pulling forces on the nucleus (Petrie et al., 2014), pushing forces may have a more dominant role in cells that exhibit a bleb-based migration phenotype, as we observe in our system.

In addition to elevated myosin-II at the cell trailing edge, actin and myosin fibers localize on the apical and basal surfaces of the nucleus to deform the nucleus in the dorsoventral direction. Previous studies have demonstrated that pressurization of the nucleus, either by actin deformation or physical confinement, results in nuclear envelope bleb formation and rupture, specifically in areas where the nuclear lamina is not strong enough to withstand this pressure (Hatch and Hetzer, 2016; Kanellos et al., 2015; Takaki et al., 2017; Wiggan et al., 2017). When actomyosin contractility becomes unrestrained via PPP1R12A/PPP1CB or Cof/ADF depletion, this pressurization by perinuclear actomyosin induces nuclear blebbing without any directional bias on 2D surfaces (Kanellos et al., 2015; Takaki et al., 2017; Wiggan et al., 2017). Our results suggest that while perinuclear actomyosin-dependent nuclear deformation is sufficient to induce some nuclear bleb formation in wider microchannels, further pressurization of the nucleus via cortical myosin-II-dependent passive influx from the nuclear trailing edge exacerbates nuclear blebbing in tightly confined channels. In support of this, nuclear influx was significantly reduced in wider ( $W = 50 \mu\text{m}$ ) channels with a fixed height of 3  $\mu\text{m}$  as compared with four-walled, tightly confining channels ( $W \times H = 10 \times 3 \mu\text{m}^2$ ), presumably because the nucleus does not compartmentalize the cell in wider channels. Moreover, we predominantly observe blebs on the front of the nucleus, suggesting that pressure-driven flow from the cell rear into the nucleus contributes to nuclear bleb formation. Indeed, by increasing pressure at the cell anterior via the application of a hypotonic shock at the cell leading edge, blebs are formed at the nuclear trailing edge. Taken together, our data suggest synergistic roles of cortical actomyosin-mediated nuclear influx from the cell posterior and perinuclear actomyosin-dependent nuclear deformation in directional bleb formation.

In order for nuclear blebs to form, force transmission between the cytoskeleton and the nucleus via the LINC complex is critical. The LINC complex connects apical/basal actomyosin fibers to the nuclear envelope to facilitate nuclear deformation (Hatch and Hetzer, 2016; Khatau et al., 2009). Additionally, along with cytoskeletal elements, the LINC complex tethers the nucleus in place, thereby contributing to compartmentalized cellular pressure buildup (Petrie et al., 2014). Our data suggest that in the absence of the LINC complex, the nucleus is unanchored, and therefore susceptible to pressure-driven repositioning within the cell. This translocation of the nucleus in the absence of LINC-mediated anchoring relieves pressure at the cell posterior, thereby reducing nuclear influx and subsequent bleb formation. Therefore, the LINC complex may increase nuclear blebbing both by deforming the nucleus and by promoting actomyosin-induced pressure buildup at the cell posterior.

The rheological properties of the nucleus may exacerbate damage associated with nuclear bleb formation and rupture. Lamin B1 has been shown to be weak or absent from nuclear blebs (Denais et al., 2016). Nuclear blebs do not completely disappear after a rupture event but instead steadily expand in volume after each sequential repair. Along these lines, other studies have reported that nuclear blebs formed on 2D as a result of Cof/ADF depletion retracted slowly relative to their rapid formation (Wiggin et al. 2017). This is consistent with reports that isolated nuclei behave as viscoelastic solids (Guilak et al., 2000) and that nuclei experience irreversible deformation after pressure is applied by micropipette aspiration (Cao et al., 2016; Pajeroski et al., 2007). Our results suggest that the plastic nature of the nucleus may prevent retraction of nuclear blebs. Instead, continuous pressurization of the nucleus via actomyosin contractility induces progressively larger deformations of the nuclear envelope. Additionally, nuclear blebs are devoid of nuclear pores as shown previously (Denais et al., 2016). Although the exact mechanism of this remains unknown, it is likely that the absence of nuclear pores locally suppresses nuclear efflux and may contribute to the observed increase of nuclear bleb size. Along these lines, our results demonstrate that nuclear efflux inhibition increases nuclear volume and nuclear blebbing both in confinement and on 2D. Together, these factors promote numerous uncontrolled rupture events, which have negative consequences for genomic integrity.

Nuclear rupture has been shown to induce DNA damage via chromatin herniation and DNA repair factor mislocalization into the cytoplasm (Denais et al., 2016; Irianto et al., 2017; Raab et al., 2016). However, our results suggest that confinement elevates passive nuclear influx, which may disrupt the homeostatic balance of the nucleus and induce DNA damage through other pathways. With a threshold of ~40 kD for passive nuclear influx (Stewart, 2007), water, small macromolecules, and numerous ionic species could be pushed into the nucleus during confined migration. Alteration of the osmolarity of the nucleus by these means could disrupt the biochemical interactions of nuclear proteins (Cao et al., 2016). Confinement of cells has also been shown to segregate DNA repair factors away from the nucleus even in the absence of nuclear rupture (Irianto et al., 2016), suggesting that genomic damage caused by nuclear influx might be exacerbated by depletion of these factors.

In view of a direct link between nuclear rupture and DNA damage (Denais et al., 2016; Raab et al., 2016), cell migration through constricted tissue microenvironments may have profound consequences on genomic integrity, cell fate, and cancer evolution (Irianto et al., 2017). Our findings may have broad implications in cancer metastasis. Our data reveal that deregulation of the homeostatic balance of nuclear influx and efflux (influx > efflux) is sufficient to support both nuclear bleb formation and nuclear volume expansion, and concomitantly suppress cancer cell motility. Along these lines, we have discovered that inhibition of active nuclear export using an exportin 1 inhibitor or TPR knockdown reduces passive nuclear efflux, which induces nuclear bleb formation on 2D and in confinement. Interestingly, inhibitors of nuclear export have shown promising preclinical results and are currently being evaluated in clinical trials as tumor suppressors. Although these results are primarily attributed to the reduction of tumor growth (Stelma et al., 2016), we suggest that these inhibitors may also disrupt nuclear integrity and interfere with metastatic spread due to increased nuclear size and concomitant decreased cell migration/invasion.

Distinct physical cues as well as nuclear expansion may exert divergent effects on chromatin organization, ultimately resulting in differential regulation of the epigenome and transcriptome, and triggering persistent long-term genotoxic effects on cell function. Overall, our work provides additional insight into the processes of nuclear bleb formation and rupture, which could aid in the development of novel therapeutics to combat metastasizing cancer cells that experience this phenomenon.

## Materials and methods

### Experimental methods

#### Cell culture and pharmacological inhibitors

Human HT-1080 fibrosarcoma cells (kindly provided by D. Wirtz, Johns Hopkins University, Baltimore, MD) and HOS cells were cultured in DMEM containing 4.5 g/l glucose, L-glutamine, and sodium pyruvate (Gibco) and supplemented with 10% heat inactivated FBS (Gibco) and 1% penicillin/streptomycin (10,000 U/ml; Gibco). Cells were grown in an incubator maintained at 37°C and 5% CO<sub>2</sub>, and passaged every 2–4 d.

In select experiments, cells were treated with the following pharmacological agents (obtained from Sigma-Aldrich unless otherwise noted) and corresponding VCs: Y27632 (10 μM), blebbistatin (50 μM), lysophosphatidic acid (50 μM), CN03 Rho activator (Cytoskeleton, Inc., 1 μg/ml), C3 Transferase Rho inhibitor (Cytoskeleton, Inc., 2 μg/ml), and LMB (Cell Signaling, 5, 10, or 20 nM).

#### Cloning, lentivirus preparation, transduction, and transfection

To generate shRNA lentiviral vectors, we subcloned the target sequences into pLVTHM (Addgene; plasmid 12247) using MluI and ClaI as restriction sites. The target sequences are as follows: scramble control: sh1 (5'-GCACTACCAGAGCTAACTCAGATAGTACT-3'), human MYH9 (5'-ACGGAGATGGAGGACCTTATG-3'), and human MYH10 (5'-GGATCGCTACTATTCAGGA-3').

Lentiviral shRNA targeting human SUN1 and SUN2 was generously given by the Burrige Lab (University of North

Carolina at Chapel Hill, Chapel Hill, NC; [Guilluy et al., 2014](#)). GFP-lamin-A (pCDH-CMV-BlastiS-P2A-prelamin-A) was generously given by the Lammerding Lab (Cornell University, Ithaca, NY; [Denais et al., 2016](#)). The following plasmids were purchased from Addgene: pLenti.PGK.LifeAct-Ruby.W (plasmid 51009), pLenti.PGK.H2B-mCherry (plasmid 51007), MYH9-GFP (plasmid 11347), MYH10-mCherry (plasmid 55107), tetO-FUW-eGFP-RHOA-Q63L (plasmid 73081), tetO-FUW-eGFP (plasmid 73083), FUDeltaGW-rtTA (plasmid 19780), RhoA2G FRET biosensor (plasmid 40176, 40179), psPAX2 (plasmid 12260), pMD2.G (plasmid 12259), mCherry-NUP50-N-10 (plasmid 55111), and PA-GFP (plasmid 18697).

The lentiviral plasmid for the expression of the NLS-GFP-MBP-NES(Rev) nuclear transport reporter (pK542) was prepared by sequential cloning of synthetic oligonucleotides and PCR products into pLenti V5-D TOPO (Invitrogen). The reporter contains the N-terminal NLS sequence of SV40 Large T-antigen (PKKRKV) and the C-terminal NES of Rev (LPPLERLTL) that were added to GFP-tagged maltose binding protein (MBP) from *Escherichia coli*. The lentiviral plasmid for the expression of the NLS-GFP-MBP-NES(Survivin) nuclear transport reporter (pK561) was prepared as described above but containing C-terminal NES of Survivin (VKKQFEELTL). NES from Rev is stronger than NES from Survivin ([Fetz et al., 2009](#)), causing pK542 to localize predominately in the cytoplasm while allowing pK561 to localize in both the cytoplasm and nucleus.

For lentivirus production, 293T/17 cells were cotransfected with psPAX2, pMD2.G, and the lentiviral plasmid. Lentivirus was harvested 48 h after transfection and was purified via centrifugation (50,000 *g* for 2 h at 4°C). Subsequently, cells were transduced for 24 h with media containing lentiviral particles.

For siRNA knockdown, scramble (sc-37007) and TPR (sc-45343) siRNA were purchased from Santa Cruz Biotechnology. Cells were transiently transfected with siRNA using the Lipofectamine RNAiMax Kit (Invitrogen) according to the manufacturer's protocol.

For transient transfections, 60–80% confluent HT-1080 cells were transfected using Lipofectamine 3000 reagent using the manufacturer's recommendations.

### Photolithography and device fabrication

Polydimethylsiloxane-based microfluidic devices, which consist of an array of parallel channels with a fixed channel length of 200  $\mu\text{m}$ , a fixed height of 3  $\mu\text{m}$ , and widths of 10  $\mu\text{m}$  or 50  $\mu\text{m}$ , were fabricated as described previously ([Balzer et al., 2012](#); [Hung et al., 2016](#); [Paul et al., 2016](#)). Confinement was applied by inducing cells to migrate through a channel with a height of 3  $\mu\text{m}$  and a width of 10  $\mu\text{m}$ . The heights of all channels were verified using a profilometer. For cell migration experiments, channels were coated with 20  $\mu\text{g}/\text{ml}$  collagen I (Collagen I Rat Protein, Tail; Thermo Fisher Scientific).

### Microfluidic device seeding and live cell imaging

Cells were detached from culture dishes using 0.05% trypsin-EDTA (Gibco), centrifuged at 300 *g* for 5 min, and resuspended in DMEM (1% penicillin/streptomycin, no FBS) to a concentration of  $5 \times 10^6$  cells/ml. 10–20  $\mu\text{l}$  of cell suspension was then

added to the device inlet, generating a pressure driven flow of cells into the device. Cells were allowed to adhere and spread outside of the channel entrances for at least 5 min. The four inlet wells of the device were then filled with 100  $\mu\text{l}$  media. The bottom three wells were filled with DMEM (no FBS and 1% penicillin/streptomycin), while the top well was filled with DMEM (10% FBS and 1% penicillin/streptomycin) to create a chemotactic gradient within the device. Devices were incubated at 37°C and 5% CO<sub>2</sub> before imaging.

Cells were imaged for every 30 s to 20 min for 4 to 12 h on an inverted Nikon Eclipse Ti microscope (Nikon) with automated controls (NIS-Elements; Nikon) and a  $\times 10/0.45$  NA Ph1 objective using time-lapse microscopy. During the experiments, cells were maintained on a temperature and CO<sub>2</sub> controlled stage top incubator (Okolab or Tokai Hit). For select experiments, cells were imaged using FITC and TRITC filters.

### Cell migration tracking and analysis

Live cell videos were exported to ImageJ (National Institutes of Health). The Manual Tracking (F. Cordelières, Institut Curie, Orsay, France) and MTrackJ ([Meijering et al., 2012](#)) plugins were used for cell path tracking. Cell paths were recorded from the time of complete entry into the microchannel until contact was made with the end of the microchannel. A custom-made MATLAB (MathWorks) script was used to calculate cell speed from the cell path. Dividing or apoptotic cells were excluded from analysis. For each condition,  $\sim 30$  cells were analyzed for each of three or more independent trials unless otherwise noted.

For nuclear blebbing classification, cells were observed with an inverted Nikon Eclipse Ti microscope (Nikon) using a 40 $\times$  air objective. Nuclear blebbing was tabulated manually.

### Actin and nucleus staining

Cells were fixed with 4% paraformaldehyde (Affymetrix), permeabilized in 0.1% Triton X-100 (Sigma-Aldrich), and blocked in 1% bovine serum albumin. Cells were stained with rhodamine or Alexa Fluor 488 phalloidin (1:100; Invitrogen) and Hoechst (1:2,500; Invitrogen).

### Confocal imaging

Cells were imaged using a Zeiss LSM 700 confocal microscope (Carl Zeiss MicroImaging) and a Nikon A1 confocal microscope (Nikon) using a 60/63 $\times$  oil objective with a 1.4 NA and a resolution of  $1,024 \times 1,024$  pixels. During the experiments, cells were maintained on a temperature and CO<sub>2</sub> controlled stage top incubator (Okolab). A 567-, 488-, or 405-nm laser was used for imaging.

Super resolution imaging was performed with Zeiss LSM 800 Confocal with AiryScan super-resolution module with x,y resolution of 120 nm and z resolution of 350 nm.

### PA-GFP imaging

HT-1080 cells were transfected with PA-GFP as described above. Cells were imaged using the FRAP capabilities of a Nikon A1 confocal microscope (Nikon) with a 60 $\times$  oil objective. Cells were stimulated for 1 s using UV-violet light (405-nm) at 2% intensity, then imaged. For nuclear influx and efflux, images were taken



for 4 min at 1-s intervals using a 488-nm laser with a resolution of  $512 \times 512$  pixels. For measurements of PA-GFP transport inside the nucleus, images were taken for 20 s at 0.25-s intervals using a 488-nm laser with a resolution of  $256 \times 256$  pixels.  $t_{1/2}$  values were calculated using curve fitting tools in GraphPad Prism 6 and 7 Software based on the equations:

$$\begin{aligned} \text{Influx: } Y &= Y_0 + (\text{Plateau} - Y_0) \times [1 - \exp(-K \times t)] \\ \text{Efflux: } Y &= (Y_0 - \text{Plateau}) \times \exp(-K \times t) + \text{Plateau}, \end{aligned}$$

where  $Y$  is intensity in arbitrary units and  $t$  is time in seconds,  $Y_0$  is the intensity when time is zero,  $\text{Plateau}$  is the intensity value at long times,  $K$  is the rate constant expressed in  $\text{s}^{-1}$ , and  $t_{1/2}$  is in seconds. The  $t_{1/2}$  is computed as  $\ln(2)/K$ . Ruptured nuclei were excluded from the calculations of nuclear influx and efflux rates.

### Osmotic shock experiments

Osmotic shocks were applied as described previously (Stroka et al., 2014). Briefly, hypotonic solutions were prepared by diluting DMEM twofold (165 mOsm) or fourfold (85.5 mOsm) with ultra-pure water. Hypertonic solutions (620 mOsm) were prepared by adding 4% xylose to DMEM. The osmolarity of each solution was measured using freezing point depression with an 3205 Single-Sample Osmometer (Advanced Instruments). After device seeding, cells were allowed to migrate through the confined channels for 2–4 h before application of osmotic shock. Prior to imaging, media in inlets of the microfluidic device was replaced with isotonic, hypotonic, or hypertonic media, as appropriate.

For nuclear influx experiments, cell imaging began 10 min after osmotic shock application and was stopped 50 min after osmotic shock application.

For nuclear blebbing experiments, cells were fixed 2 h after hypotonic shock application.

### Actin cortex photoablation

For ablation experiments, cells were seeded into collagen-coated devices 4 h before ablation as described above. 10 mM Hepes (Gibco) was added to growth media. During ablation experiments, cells were maintained at 37°C. Cells were imaged through a  $40\times/\text{NA} 1.1$  water immersion objective (421867-9970-000; Carl Zeiss Imaging) using a 488-nm laser to image PA-GFP and a 561-nm laser to image Lifeact-Ruby at 1-s intervals for 4 min on a Zeiss LSM880 inverted confocal/multiphoton microscope (Carl Zeiss Imaging). Cells were ablated after 6 s at defined  $2 \times 2\text{-}\mu\text{m}$  regions at the posterior actin cortex using a 780 nm, two-photon laser produced by a Spectra Physics Insight multiphoton excitation source (MKS Instruments). Maximum laser power during experiments varied between 950 mW and 1,000 mW, and ablation was performed at 30% attenuation. Simultaneous to the laser ablation, cells were excited in the same region by a 405-nm laser at 5% attenuation in order to induce activation of PA-GFP. Laser power settings were optimized so that the ablation would disrupt the actin cortex at the cell rear, but leave the cell membrane intact so that the cell may recover after ablation. Ablations were considered successful if the targeted region formed a bleb in response to ablation, but the GFP signal remained contained within the cell body. Cells that showed GFP

escaping from the cell membrane and cells that did not bleb in response to ablation were excluded from the final analysis.

### Nuclear size and volume measurements

Cells were imaged using a Zeiss LSM 800 or Nikon A1 confocal microscope equipped with a  $63\times/60\times$  oil-immersion, 1.2/1.4 (NA) objective. A 567-nm laser was used to image cells whose nuclei were fluorescently labeled with H2B-mCherry. Images were acquired with a resolution of  $1,024 \times 1,024$  pixels. Confocal image slices were spaced 0.5 or 1  $\mu\text{m}$  apart, and the pinhole size was 1 Airy unit. The microscope was equipped with a CO<sub>2</sub> Module S (Zeiss or Tokai) and TempModule S (Zeiss) stagetop incubator (Pecon or Tokai) that was set to 37°C with 5% CO<sub>2</sub> for long-term imaging.

Nuclear volume was measured from Z-stacks using a custom MATLAB script. Out of focus z-planes were removed. Images from each analyzed focal plane were processed using the binary thresholding function in MATLAB to filter out noise. The nuclear boundary was detected in each image using the Canny Edge Detector operator. The edge was dilated and refilled as to obtain the cross-sectional area of each slice. The volume was calculated by multiplying the average area from two adjacent slices by the z-interval and integrating all values.

### FRET-based RhoA activity measurements

Transiently transfected HT-1080 cells expressing the RhoA2G biosensor were chosen for imaging. For both confined and unconfined cells, images at CFP (excitation: 430/24, emission: 470/24), YFP (excitation: 500/20, emission: 535/30), and FRET (excitation: 430/24, emission: 535/30) settings were acquired. For quantification, the mean pixel ratio of FRET over CFP was considered after corresponding background subtraction and outlining the cell boundary by tracing the YFP image (Hung et al., 2016). For both the imaging and quantification purposes, Nikon Elements was used.

### FLIM of RhoA FRET sensors

Confocal FLIM of live cells that were stably expressing the RhoA2G sensor (Fritz et al., 2013) was performed with the use of Zeiss LSM 780 microscope and a PicoQuant system consisting of the PicoHarp 300 time-correlated single photon counting module, two hybrid PMA-04 detectors, and Sepia II laser control module. During imaging, cells were maintained in a Tecon environmental chamber at 37°C and 5% CO<sub>2</sub>.

The FLIM data were collected with Apochromat  $40\times/1.1\text{W}$  Corr 27 lens (Zeiss), using the 440-nm diode laser pulsed at 32 MHz and passed through a 440/488/640-nm triple dichroic mirror (Zeiss) for excitation. A reflection plate diverted the emission to the  $482 \pm 35\text{-nm}$  filter and PicoQuant PMA-04 hybrid detector. The pinhole size was set to acquire data from 3- $\mu\text{m}$  z-sections, or reduced (up to 1.5  $\mu\text{m}$  z) to limit the emission photon count rate below 10% of the laser excitation rate. Cells migrating in the channels were imaged within a single scan of a  $200 \times 2,000\text{-pixel}$  window, using 51.67  $\mu\text{s}$  pixel dwell time (48.4 s total scan time). Cells in 2D were imaged within a single scan of a  $1,024 \times 1,024\text{-pixel}$  window, using 25.21  $\mu\text{s}$  pixel dwell time (61 s total scan time). The time-correlated single photon counting data were acquired within a 31.25-ns time window separated into 8 ps time bins.

### FLIM reconvolution and image segmentation

The FLIM data were processed with SymPhoTime 64 (PicoQuant) software, using the customized script for the calculation of the internal response function from 100 data points with no smoothing. The data were binned to assure at least 500 photons per binned pixel, and a cell-specific threshold was applied to eliminate out-of-cell fluorescence. The three-exponential reconvolution was used to fit the fluorescence decays into every binned pixel. Since the RhoA FRET sensor was excluded from the nucleus, resulting in low and variable photon counts in the center of the cells, rectangular areas encompassing the nucleus and cytoplasm alongside the nucleus were excluded during FLIM segmentation.

### Segmentation quantification

For FLIM segmentation quantification, the SymPhoTime 64 was used to calculate the intensity-weighted fluorescence lifetime averages ( $\tau_{AI}$ ) in different areas of the cells. Manually drawn regions of interest were drawn to select areas with locally increased RhoA sensor FRET in the front or back of the cells. In cells lacking detectable local RhoA activation, the areas corresponding to one third of the distance from the leading or trailing edge to the nucleus were selected to calculate the  $\tau_{AI}$  in the front or back of cells, respectively. The remainder of the cytoplasmic areas was defined as cell center and the sum of all cytoplasmic areas as the whole cell signal.

### Myosin-II quantification

Myosin-IIA and -IIB intensity profiles were obtained using a custom MATLAB script. For each cell, line scan intensity profiles were obtained and averaged from 20 lines across the cell. Intensity from all cells was compiled, and the curve was smoothed by calculating the moving average (200 points of window size per data sample of 2 million data points). SD was calculated using the Moving Standard Deviation function in MATLAB.

### Western blotting

Western blots were performed as previously described (Chen et al., 2013; Wang et al., 2012) using NuPage 3–8% or 4–12% gels and the following antibodies.

**Primary antibodies.** Primary antibodies were anti-SUN1 antibody (produced in rabbit; Abcam; ab124770; 1:1,000), anti-SUN2 antibody (rabbit; Abcam; ab124916; 1:1,000), anti-MIIA antibody (rabbit; Sigma-Aldrich; M8064; 1:1,000), and anti-MIIB antibody (N-17; goat; Santa Cruz Biotechnology; SC-47205; 1:7,500).  $\beta$ -Actin was used as a loading control (Purified Mouse Anti-Actin Ab-5; BD Biosciences; 612656; 1:10,000).

**Secondary antibodies.** Secondary antibodies were anti-mouse IgG, HRP-linked Antibody (Cell Signaling; 7076S; 1:2,000), anti-rabbit IgG, HRP-linked antibody (Cell Signaling; 7074S; 1:2,000), and donkey anti-goat IgG-HRP (Santa Cruz Biosciences; sc-2020; 1:2,000).

### Statistical analysis

Data represent the mean  $\pm$  SEM or SD from three or more independent experiments for each condition unless stated otherwise. A Student's *t* test, a one-way or two-way ANOVA test followed by a Tukey's test for multiple comparisons, a two-way

ANOVA test followed by a Sidak's test for multiple comparisons, or a Wilcoxon matched-pairs signed rank test was used to determine statistical significance as appropriate. Statistical significance was identified as  $P < 0.05$ . Analysis was performed using GraphPad Prism 6 and 7 Software.

### Theoretical methods

Here we present a model of cell migration in confinement. The model was motivated by the experimental observation that nuclear volume expands during cell migration in confinement. We sought to model the effect such nuclear volume changes would have on cell motility. The cell and nucleus experience forces from both cytoplasmic flow in the perinuclear space and the cell's actin network. This model takes all of these forces into account to predict cell migration speed in confinement based on nuclear size. The components of this model are described below.

Since we are considering cell migration in confined channels, this model is one-dimensional except for the flow in the perinuclear space that separates the nucleus from the cell membrane. The coordinate system of the cell is shown in Fig. S6 i, where the *x*-direction is aligned with the length of the cell. The positive direction of the coordinate system points in the direction of cell migration. Let *H*, *W*, and *L* be the height, width, and length, respectively, of the cell in a channel (Fig. S6 i). We also assume that the geometry of the cell inside the channel is the same as the channel, i.e., the cell membrane always attaches to the channel wall. *H* and *W* are different for different channel geometries. We denote  $D_L$  ( $D_V$ ) as the distance separating the nucleus from the cell membrane in the lateral (vertical) direction. In general,  $D_L$  and  $D_V$  may vary slightly in space as a function of *x*. The effect of varying  $D_L$  and  $D_V$  can be incorporated in the model, but here we use constant values to approximate the effective perinuclear space. We assume that the distance separating the nucleus and the plasma membrane is the same on each opposite side of the nucleus. Hence, the height, width, and length of the nucleus can be denoted as  $H_\zeta = H - 2D_V$ ,  $W_\zeta = W - 2D_L$ , and  $L_\zeta$ , respectively. Hereafter we will use subscript *L* to refer to any quantity associated with the lateral perinuclear spaces, *V* for the vertical perinuclear spaces, and  $\zeta$  for the nucleus. As can be seen in a cross-sectional view of the cell (Fig. S6 i), the perinuclear space forms four thin canals through which fluid can pass. The width of these canals,  $D_L$  and  $D_V$ , largely affects the fluid viscous drag on the nucleus and the cell membrane.

Let  $v_0$  be the velocity of cell migration obtained from live cell imaging. Note that this apparent velocity does not necessarily equal the velocity of the lipid bilayer of the cell membrane relative to the channel wall because vesicle trafficking can also contribute to the velocity of cell migration.  $v_m$  is the velocity of the lipid bilayer relative to the channel wall and  $v_{tk}$  is the portion of the velocity of cell migration contributed by vesicle trafficking. The velocity of the cell then satisfies the equation

$$v_0 = v_m + v_{tk}. \quad (1)$$

At steady-state, the nucleus has the same velocity as the apparent velocity of the cell ( $v_0$ ).

The intracellular space is compartmentalized by the presence of the nucleus (Fig. S6 i). We denote the space in front of the nucleus as the “front compartment” and the space behind the nucleus as the “back compartment.” Fluid flows between the two compartments via the perinuclear space, where the fluid pressure gradient is substantial. Compared with the fluid pressure drop inside the narrow perinuclear space, the fluid pressure, or the hydrostatic pressure, variation within the large front or back compartment is negligible. We thus assume that in each compartment, the fluid pressure is constant. We denote  $p^b$  and  $p^f$  as the constant fluid pressure at the back and front compartment of the cell, respectively. Hereafter, we will use the superscript  $f$  to refer to any quantity at the front of the cell and the superscript  $b$  to refer to any quantity at the back of the cell. In addition to hydrostatic pressure, the cell contains multiple ionic species that balance the membrane potential and osmotic pressure across the cell membrane. To model the effect of osmolarity, we may assume electro-neutral ions of concentration  $c$ . Similarly, the intracellular ion concentrations in the two compartments are approximated as constants, denoted as  $c^b$  for the back and  $c^f$  for the front. The nucleus is also permeable at its two polar ends where water and small molecules may diffuse or be transported. Similarly, within the nucleus, we assume the hydrostatic pressure,  $p_\zeta$ , and the concentration of small molecules,  $c_\zeta$ , are constant in space.

The velocity of fluid flow in the perinuclear space  $v_D$  is affected by two factors: the hydrostatic pressure difference between the front and back compartments of the cell, and the velocity difference between the nucleus and the lipid membrane. To model the fluid flow in the perinuclear space, we use a generic coordinate system that follows the motion of the nucleus, i.e.,  $v_D$  is the velocity of the flow in the perinuclear space in the frame of the moving nucleus. The  $z$ -coordinate of perinuclear space is set such that the lipid membrane is at  $z = 0$  and the nuclear membrane is at  $z = D$  (Fig. S6 ii). Here we are using a generic notation for the perinuclear spaces so that  $D$  can represent either  $D_L$  or  $D_V$ . Since the separation distance is much smaller than the cell width and height, the fluid field in the perinuclear space can be modeled by the lubrication theory

$$0 = -\frac{\partial p}{\partial x} + \mu \frac{\partial^2 v_D}{\partial z^2}, \quad (2)$$

where  $p$  is the fluid pressure in the perinuclear spaces and  $\mu$  is the effective dynamic viscosity of the cytoplasm in the perinuclear space. In the frame of the nucleus, the boundary conditions for the flow is  $v_D = 0$  at  $z = D$  and  $v_D = -(v_0 - v_m)$  at  $z = 0$ . By solving Eq. 2, the velocity in each perinuclear space is expressed as

$$v_D(z) = \frac{1}{2\mu} \frac{\partial p}{\partial x} (z^2 - Dz) - \left(1 - \frac{z}{D}\right)(v_0 - v_m), \quad (3)$$

which shows that two terms contribute to the flow in the perinuclear space. The first term, coming from the pressure gradient in the perinuclear space, represents the Poiseuille flow. The second term, coming from the relative motion of the nucleus and the cell membrane, represents the Couette flow. The pressure gradient in the perinuclear space can be approximated as  $\partial p / \partial x = (p^f - p^b) / L_\zeta$ . Integrating Eq. 3 over the perinuclear distance gives the average flow velocity in the perinuclear space,

$$\bar{v}_D = -\frac{D^2}{12\mu} \frac{\partial p}{\partial x} - \frac{1}{2}(v_0 - v_m). \quad (4)$$

Using Eq. 3, the fluid viscous shear stress acting on one nuclear surface is

$$\tau_\zeta = -\mu \left. \frac{\partial v_D}{\partial z} \right|_{z=D} = \mu \left[ -\frac{D}{2\mu} \frac{\partial p}{\partial x} - \frac{1}{D}(v_0 - v_m) \right], \quad (5)$$

and the fluid viscous shear stress acting on one cell lipid membrane is

$$\tau_m = \mu \left. \frac{\partial v_D}{\partial z} \right|_{z=0} = \mu \left[ -\frac{D}{2\mu} \frac{\partial p}{\partial x} + \frac{1}{D}(v_0 - v_m) \right]. \quad (6)$$

Eqs. 5 and 6 show that the viscous shear stress on the nucleus and on the lipid membrane is not symmetric if there is vesicle trafficking, i.e.,  $v_0 \neq v_m$ . When Poiseuille flow dominates, the shear stress increases with increasing separation distance; when Couette flow dominates, the shear stress increases with decreasing separation distance. The total viscous forces on the nuclear surface,  $f_{\tau,\zeta}$ , and on the cell lipid membrane,  $f_{\tau,m}$ , are the sum of the viscous forces in each of the four spaces in the perinuclear region obtained by multiplying the shear stress with the corresponding contact area, i.e.,

$$f_{\tau,\zeta} = 2\tau_{\zeta,L}H_\zeta L_\zeta + 2\tau_{\zeta,V}W_\zeta L_\zeta, \quad (7)$$

and

$$f_{\tau,m} = 2\tau_{m,L}H_\zeta L_\zeta + 2\tau_{m,V}W_\zeta L_\zeta, \quad (8)$$

where  $\tau_{\zeta,L}$ ,  $\tau_{\zeta,V}$ ,  $\tau_{m,L}$ , and  $\tau_{m,V}$  are obtained from Eqs. 5 and 6 by replacing  $D$  with either  $D_L$  or  $D_V$ .

At steady-state, the continuity condition requires that the volumetric flow rate must be equal at each cross section throughout the cell. This provides a relationship between the volumetric flow rate in the perinuclear spaces and the nucleus to the volumetric flow rate at the cell boundaries, i.e.,

$$2D_L H_\zeta \bar{v}_{D,L} + 2D_V W_\zeta \bar{v}_{D,V} + H_\zeta W_\zeta J_{\zeta,\text{water}}^b = HW J_{\text{water}}^b, \quad (9)$$

and at steady-state, conservation of mass requires that

$$J_{\text{water}}^f = -J_{\text{water}}^b \quad (10)$$

and

$$J_{\zeta,\text{water}}^f = -J_{\zeta,\text{water}}^b, \quad (11)$$

where  $J_{\text{water}}$  and  $J_{\zeta,\text{water}}$ , defined positive inwards, are the water flux (in the units of m/s) across the cell and nuclear membranes, respectively, at the front and back. The flux is proportional to the difference of the chemical potential of water (hydrostatic pressure minus osmotic pressure) across each membrane, i.e.,

$$J_{\text{water}}^{f/b} = -\alpha^{f/b} \left[ (p^{f/b} - p_0^{f/b}) - RT(c^{f/b} - c_0^{f/b}) \right] \quad (12)$$

and

$$J_{\zeta,\text{water}}^{f/b} = -\alpha_\zeta^{f/b} \left[ (p_\zeta - p^{f/b}) - RT(c_\zeta - c^{f/b}) \right], \quad (13)$$

where  $\alpha$  is the coefficient of water permeation of the membrane and the subscript 0 refers to quantities associated with the

extracellular space. Small molecules can diffuse in and out of the nucleus through the nucleus pores. We can let  $J_{c_s}^{f/b} = -g_s^{f/b}(c_s - c^{f/b})$  be the influx of small molecules into the nucleus from the front and back of the nucleus, where  $g_s$  is the coefficient of diffusion. Under steady-state, the total flux must be conserved, i.e.,

$$g_s^b(c_s - c^b) + g_s^f(c_s - c^f) = 0. \quad (14)$$

In addition to the forces from the fluid flow, the nucleus and the cell membrane are also balanced by forces from the actin network, which in this model consists of forces from actin polymerization and myosin contraction. Actin polymerization and depolymerization occur at both the front and back compartments of the cell. We assume that collectively, actin is polymerized at the cell membrane (the plus end; see Fig. S6 iii) and depolymerized at the nuclear membrane (the minus end). Of note, this represents the net effect of actin dynamics in each compartment and should not be interpreted as the dynamics of a single F-actin, as one F-actin filament is much shorter than the length of the compartments. Actin does not extend freely in space upon polymerization but pushes against the cell membrane and the nuclear membrane, generating forces on these two membranes. We will take the actin filaments at the back compartment of the cell as an example to derive a force balance; equations at the front of the cell follow the same rationale. The actin filaments exert pushing force,  $f_{\text{actin}}^b$ , on the back of the cell membrane (Fig. S6 iii), and at the same time the cell membrane exerts the same force in the opposite direction on actin (Fig. S6 iv). Similarly, a pair of forces,  $f_{\text{actin}}^b$ , are exerted at the interface between the actin and the nuclear membrane. The rate of polymerization,  $k_{\text{on}}^b$ , depends on the force acting on the filament and decreases with increasing force. The rate of depolymerization,  $k_{\text{off}}^b$ , on the other hand, increases with the force acting on the filament. As a linear approximation, these two rates can be written as

$$k_{\text{on}}^b(f_{\text{actin}}^b) = -\frac{K_{\text{on}} f_{\text{actin}}^b}{F_{\text{on}}} + K_{\text{on}}, \quad k_{\text{off}}^b(f_{\text{actin}}^b) = \frac{K_{\text{off}} f_{\text{actin}}^b}{F_{\text{off}}} + K_{\text{off}}, \quad (15)$$

where  $K_{\text{on}}$  and  $K_{\text{off}}$  are the maximum rates of polymerization and depolymerization, respectively; and  $F_{\text{on}}$  and  $F_{\text{off}}$  are the cutoff forces of polymerization and depolymerization, respectively. Under steady-state, where the actin length is constant, the rates of polymerization and depolymerization must be equivalent, i.e.,  $k_{\text{on}}^b = k_{\text{off}}^b$ , which solves  $f_{\text{actin}}^b$  as a function of  $f_{\text{actin}}^b$ ,

$$f_{\text{actin}}^b = -\frac{F_{\text{off}} K_{\text{on}} f_{\text{actin}}^b}{F_{\text{on}} K_{\text{off}} f_{\text{actin}}^b + F_{\text{off}} K_{\text{on}}} + \frac{F_{\text{off}} K_{\text{on}}}{K_{\text{off}}}. \quad (16)$$

In the frame of the moving cell, the continuous actin polymerization leads to a retrograde flow with velocity (defined positive toward the positive  $x$ -direction):  $v_{\text{actin}} = k_{\text{on}}^b \Delta = k_{\text{off}}^b \Delta$ , where  $\Delta$  is the effective size of a G-actin monomer. The fluid velocity in the back compartment of the cell is given by  $J_{\text{water}}^b$ . The difference of the two velocities gives rise to a viscous force on the actin filament (defined positive toward the positive  $x$ -direction), i.e.,

$$f_{\mu, \text{actin}}^b = -\mu_{\text{actin}}(v_{\text{actin}}^b - J_{\text{water}}^b), \quad (17)$$

where  $\mu_{\text{actin}}$  is the coefficient of viscous drag between the fluid and actin filament. The force balance of the actin filament at the back compartment of the cell is (Fig. S6 iv)

$$f_{\text{actin}}^b + f_{\mu, \text{actin}}^b = f_{\text{actin}}^b. \quad (18)$$

Similarly, the force balance of the actin filaments at the front compartment is

$$f_{\text{actin}}^f + f_{\mu, \text{actin}}^f = f_{\text{actin}}^f, \quad (19)$$

where

$$f_{\text{actin}}^f = -\frac{F_{\text{off}} K_{\text{on}}}{F_{\text{on}} K_{\text{off}}} f_{\text{actin}}^f + \frac{F_{\text{off}} K_{\text{on}}}{K_{\text{off}}}, \quad (20)$$

and

$$f_{\mu, \text{actin}}^f = -\mu_{\text{actin}}(k_{\text{on}}^f \Delta - J_{\text{water}}^f), \quad (21)$$

in which

$$k_{\text{on}}^f = -\frac{K_{\text{on}} f_{\text{actin}}^f}{F_{\text{on}}} + K_{\text{on}}. \quad (22)$$

Myosin is mostly distributed at the two polar ends of the cell and provides contraction forces on the membrane. We denote  $\sigma_{\text{myosin}}$  as the effective contraction stress from myosin. Each myosin has two ends. One pulls the cell membrane inwards and the other is anchored to a cytoskeleton network that effectively spreads over the cell lateral and vertical membranes. The effective contractile force from the myosin on the cell membrane at the back and front is  $f_{\text{myosin}} = \sigma_{\text{myosin}} HW$ .

With all the major forces considered, the force balance of the back membrane can be written as (Fig. S6 iii)

$$(p^b - p_0^b)HW + f_{\text{actin}}^b = 2(H + W)T_m^b + HW\sigma_{\text{myosin}}^b, \quad (23)$$

where  $T_m^b$  is the cell membrane tension at the back. Similarly, the force balance at the front membrane is

$$(p^f - p_0^f)HW + f_{\text{actin}}^f = 2(H + W)T_m^f + HW\sigma_{\text{myosin}}^f, \quad (24)$$

where  $T_m^f$  is the cell membrane tension at the front. Here we can see that the forces of the actin filaments are coupled to the forces from myosin in an implicit way through the force balance of the cell membrane. The force balance of the entire cell membrane is (Fig. S6 iv)

$$(p^b - p^f)HW + (f_{\text{actin}}^b - f_{\text{actin}}^f) + 2L(H + W)\xi_m v_m = f_{\tau, m}, \quad (25)$$

where  $\xi_m$  is the coefficient of friction between the cell membrane and the channel wall; the corresponding term accounts for the frictional force on the cell membrane due to the membrane velocity  $v_m$ . Note that myosin contraction does not go into the force balance of the entire membrane because the forces on the two ends and on the membranes attached to the channel walls are balanced and the net effect vanishes. We also need to establish a force balance for the nucleus (Fig. S6 iv):



Table 1. Lists of parameters

Parameters	Descriptions	Values
$R$ (J/mol K)	Ideal gas constant	8.31451
$T$ (K)	Absolute temperature	300
$L$ ( $\mu\text{m}$ )	Cell length	80
$W$ ( $\mu\text{m}$ )	Channel width	10
$H$ ( $\mu\text{m}$ )	Channel height	10
$\mu$ (Pa s)	Dynamic viscosity of the cytoplasm	0.005
$\mu_{\text{actin}}$ (Pa s)	Coefficient of friction of the actin filament	0.01
$\xi_m$ (Pa s/m)	Coefficient of friction between the cell membrane and the channel wall	$3.7 \times 10^6$
$p_0^{b/f}$ (Pa)	Extracellular hydrostatic pressure	0
$c_0^{b/f}$ (mM)	Extracellular osmolarity	0
$c^b$ (mM)	Intracellular osmolarity at the back	1
$\alpha^{b/f}$ (m/Pa s)	Water permeability of the cell membrane	$8 \times 10^{-11}$
$\alpha_z^{b/f}$ (m/Pa s)	Water permeability of the nuclear membrane	$1 \times 10^{-12}$
$g_z^{b/f}$ ( $\mu\text{m/s}$ )	Coefficient of effective diffusion constant at the nuclear membrane	100
$v_{\text{tk}}^0$ ( $\mu\text{m/s}$ )	Maximum rate of vesicle trafficking when $T_m = 0$	0.1
$T_{\text{max}}$ (N/s)	Maximum membrane tension that stalls vesicle trafficking	0.01
$F_{\text{on}}$ (nN)	Cut-off force for actin polymerization	50
$F_{\text{off}}$ (nN)	Cut-off force for actin depolymerization	6
$K_{\text{on}}$ (1/s)	Maximum rate of actin polymerization	3
$K_{\text{off}}$ (1/s)	Maximum rate of actin depolymerization	3
$\Delta$ (nm)	Effective size of a G-actin	3
$\sigma_{\text{myosin}}^b$ (Pa)	Effective contraction stress from myosin at the back	4,500
$\sigma_{\text{myosin}}^f$ (Pa)	Effective contraction stress from myosin at the front	1,000

$$(p^b - p^f)H_\zeta W_\zeta + (f_{\text{actin}}^b - f_{\text{actin}}^f) + f_{\tau_s} = 0. \quad (26)$$

Vesicle trafficking (the net effect of on-rate and off-rate) happens at both ends of the cell, the difference of which determines  $v_{\text{tk}}$ , i.e.,  $v_{\text{tk}} = v_{\text{tk}}^b - v_{\text{tk}}^f$ . The rate of vesicle trafficking is related to the membrane tension,  $T_m$ . We assume a linear relation such that when  $T_m = 0$  the rate of trafficking reaches the maximum,  $v_{\text{tk}}^0$ , and when the membrane tension reaches the maximum,  $T_{\text{max}}$ , the trafficking stops. Therefore,  $v_{\text{tk}}$  can be written as

$$v_{\text{tk}} = v_{\text{tk}}^b - v_{\text{tk}}^f = v_{\text{tk}}^0 \left(1 - \frac{T_m^b}{T_{\text{max}}}\right) - v_{\text{tk}}^0 \left(1 - \frac{T_m^f}{T_{\text{max}}}\right). \quad (27)$$

In this model,  $c^b$  and  $\sigma_{\text{myosin}}$  are given while  $p^b$ ,  $p^f$ ,  $c^f$ ,  $T_m^b$ ,  $T_m^f$ ,  $v_0$ ,  $v_m$ ,  $f_{\text{actin}}^b$ ,  $f_{\text{actin}}^f$ ,  $p_\zeta$ , and  $c_\zeta$  are solved from Eqs. 1, 9, 10, 11, 14, 18, 19, 23, 24, 25, and 26. All of these equations are coupled.

The parameters used in the model are listed in Table 1. We vary  $H_\zeta$  linearly from 2  $\mu\text{m}$  to 2.5  $\mu\text{m}$ ,  $W_\zeta$  from 8  $\mu\text{m}$  to 9.5  $\mu\text{m}$ , and  $L_\zeta$  from 18  $\mu\text{m}$  to 70  $\mu\text{m}$ .

### Online supplemental material

Fig. S1 (related to Fig. 1) illustrates the extent of nuclear blebbing inside channels and on 2D for HT-1080 and HOS cells, provides additional characterization of nuclear rupture in confinement, and demonstrates the effect of ROCK/myosin-II inhibition on

nuclear blebbing/rupture as well as the extent of myosin-IIA/B and SUN1/2 shRNA knockdowns. Fig. S2 (related to Fig. 2) shows control experiments for the RhoA2G biosensor. Fig. S3 (related to Fig. 3) shows additional data demonstrating that nuclear influx, but not efflux, is elevated in confinement, but not on 2D. Fig. S4 (related to Fig. 4) shows data demonstrating the effects of LMB treatment and TPR depletion on nuclear influx and efflux as well as verification of siTPR knockdown. Fig. S5 (related to Fig. 5) includes additional data depicting the kinetics of nuclear volume expansion for bleb-bearing and bleb-free nuclei. Fig. S6 (related to Fig. 5) shows a schematic overview of the mathematical model.

### Acknowledgments

The authors would like to thank Martin Rietveld for his help with the schematic representation of the proposed model.

This work was supported, in part, by a National Science Foundation Graduate Research Fellowship (DGE-1746891 to E.O. Wisniewski), an American Heart Association Postdoctoral Fellowship (18POST34080345 to P. Mistryotis), and grants from the National Institutes of Health (R01CA183804 to K. Konstantopoulos, R01CAGM114675 to S.X. Sun and K. Konstantopoulos, U54CA210173 to K. Konstantopoulos and S.X. Sun, and R01HL082792 and

U54CA210184 to J. Lammerding), the U.S. Department of Defense Breast Cancer Research Program (Breakthrough Award BC150580 to J. Lammerding), and the National Science Foundation (CAREER Award CBET-1254846 to J. Lammerding). Some of the imaging data were acquired through the Cornell University Biotechnology Resource Center, with NYSTEM (CO29155) and National Institutes of Health (S10OD018516) funding for the shared Zeiss LSM880 confocal/multiphoton microscope. This work received additional support from the Knight@KIC 2018-2019 Graduate Fellowship (to J. Keys).

The authors declare no competing financial interests.

Author contributions: P. Mistriotis and E.O. Wisniewski designed the study, performed most experiments, analyzed data, and wrote the manuscript. K. Bera, S. Tuntithavornwat, R.A. Law, N. Perez, E. Erdogmus, Y. Zhang, and R. Zhao performed select experiments and analyzed data. Y.L. and S.X. Sun developed the mathematical model. J. Keys and J. Lammerding performed photoablation experiments, provided critical input, and edited the manuscript. P. Kalab provided critical input, supplied reagents, assisted with FLIM experiments, and edited the manuscript. K. Konstantopoulos designed and supervised the study and wrote the manuscript.

Submitted: 11 February 2019

Revised: 28 May 2019

Accepted: 18 September 2019

## References

- Amano, M., M. Ito, K. Kimura, Y. Fukata, K. Chihara, T. Nakano, Y. Matsuura, and K. Kaibuchi. 1996. Phosphorylation and activation of myosin by Rho-associated kinase (Rho-kinase). *J. Biol. Chem.* 271:20246–20249. <https://doi.org/10.1074/jbc.271.34.20246>
- Balzer, E.M., Z. Tong, C.D. Paul, W.C. Hung, K.M. Stroka, A.E. Boggs, S.S. Martin, and K. Konstantopoulos. 2012. Physical confinement alters tumor cell adhesion and migration phenotypes. *FASEB J.* 26:4045–4056. <https://doi.org/10.1096/fj.12-211441>
- Bangs, P., B. Burke, C. Powers, R. Craig, A. Purohit, and S. Doxsey. 1998. Functional analysis of Tpr: identification of nuclear pore complex association and nuclear localization domains and a role in mRNA export. *J. Cell Biol.* 143:1801–1812. <https://doi.org/10.1083/jcb.143.7.1801>
- Ben-Efraim, I., P.D. Frosst, and L. Gerace. 2009. Karyopherin binding interactions and nuclear import mechanism of nuclear pore complex protein Tpr. *BMC Cell Biol.* 10:74. <https://doi.org/10.1186/1471-2121-10-74>
- Buxboim, A., J. Swift, J. Irianto, K.R. Spinler, P.C. Dingal, A. Athirasala, Y.R. Kao, S. Cho, T. Harada, J.W. Shin, and D.E. Discher. 2014. Matrix elasticity regulates lamin-A,C phosphorylation and turnover with feedback to actomyosin. *Curr. Biol.* 24:1909–1917. <https://doi.org/10.1016/j.cub.2014.07.001>
- Buxboim, A., J. Irianto, J. Swift, A. Athirasala, J.W. Shin, F. Rehfeldt, and D.E. Discher. 2017. Coordinated increase of nuclear tension and lamin-A with matrix stiffness outcompetes lamin-B receptor that favors soft tissue phenotypes. *Mol. Biol. Cell.* 28:3333–3348. <https://doi.org/10.1091/mbc.e17-06-0393>
- Cao, X., E. Moeendarbary, P. Isermann, P.M. Davidson, X. Wang, M.B. Chen, A.K. Burkart, J. Lammerding, R.D. Kamm, and V.B. Shenoy. 2016. A Chemomechanical Model for Nuclear Morphology and Stresses during Cell Transendothelial Migration. *Biophys. J.* 111:1541–1552. <https://doi.org/10.1016/j.bpj.2016.08.011>
- Chen, S.H., W.C. Hung, P. Wang, C. Paul, and K. Konstantopoulos. 2013. Mesothelin binding to CA125/MUC16 promotes pancreatic cancer cell motility and invasion via MMP-7 activation. *Sci. Rep.* 3:1870. <https://doi.org/10.1038/srep01870>
- Crisp, M., Q. Liu, K. Roux, J.B. Rattner, C. Shanahan, B. Burke, P.D. Stahl, and D. Hodzic. 2006. Coupling of the nucleus and cytoplasm: role of the LINC complex. *J. Cell Biol.* 172:41–53. <https://doi.org/10.1083/jcb.200509124>
- Davidson, P.M., C. Denais, M.C. Bakshi, and J. Lammerding. 2014. Nuclear deformability constitutes a rate-limiting step during cell migration in 3-D environments. *Cell. Mol. Bioeng.* 7:293–306. <https://doi.org/10.1007/s12195-014-0342-y>
- Davidson, P.M., J. Sliz, P. Isermann, C. Denais, and J. Lammerding. 2015. Design of a microfluidic device to quantify dynamic intra-nuclear deformation during cell migration through confining environments. *Integr. Biol.* 7:1534–1546. <https://doi.org/10.1039/C5IB00200A>
- Denais, C.M., R.M. Gilbert, P. Isermann, A.L. McGregor, M. te Lindert, B. Weigelin, P.M. Davidson, P. Friedl, K. Wolf, and J. Lammerding. 2016. Nuclear envelope rupture and repair during cancer cell migration. *Science.* 352:353–358. <https://doi.org/10.1126/science.aad7297>
- Elosegui-Artola, A., I. Andreu, A.E.M. Beedle, A. Lezamiz, M. Uroz, A.J. Kosmalska, R. Oria, J.Z. Kechagia, P. Rico-Lastres, A.L. Le Roux, et al. 2017. Force Triggers YAP Nuclear Entry by Regulating Transport across Nuclear Pores. *Cell.* 171:1397–1410.e14. <https://doi.org/10.1016/j.cell.2017.10.008>
- Fetz, V., S.K. Knauer, C. Bier, J.P. von Kries, and R.H. Stauber. 2009. Translocation Biosensors - Cellular System Integrators to Dissect CRM1-Dependent Nuclear Export by Chemicogenomics. *Sensors (Basel).* 9: 5423–5445. <https://doi.org/10.3390/s90705423>
- Fritz, R.D., M. Letzelter, A. Reimann, K. Martin, L. Fusco, L. Ritsma, B. Ponsioen, E. Fluri, S. Schulte-Merker, J. van Rheenen, and O. Pertz. 2013. A versatile toolkit to produce sensitive FRET biosensors to visualize signaling in time and space. *Sci. Signal.* 6:rs12. <https://doi.org/10.1126/scisignal.2004135>
- Frosst, P., T. Guan, C. Subauste, K. Hahn, and L. Gerace. 2002. Tpr is localized within the nuclear basket of the pore complex and has a role in nuclear protein export. *J. Cell Biol.* 156:617–630. <https://doi.org/10.1083/jcb.200106046>
- Guilak, F., J.R. Tedrow, and R. Burgkart. 2000. Viscoelastic properties of the cell nucleus. *Biochem. Biophys. Res. Commun.* 269:781–786. <https://doi.org/10.1006/bbrc.2000.2360>
- Guilluy, C., L.D. Osborne, L. Van Landeghem, L. Sharek, R. Superfine, R. Garcia-Mata, and K. Burridge. 2014. Isolated nuclei adapt to force and reveal a mechanotransduction pathway in the nucleus. *Nat. Cell Biol.* 16: 376–381. <https://doi.org/10.1038/ncb2927>
- Harada, T., J. Swift, J. Irianto, J.W. Shin, K.R. Spinler, A. Athirasala, R. Diegmiller, P.C. Dingal, I.L. Ivanovska, and D.E. Discher. 2014. Nuclear lamin stiffness is a barrier to 3D migration, but softness can limit survival. *J. Cell Biol.* 204:669–682. <https://doi.org/10.1083/jcb.201308029>
- Hatch, E.M., and M.W. Hetzer. 2016. Nuclear envelope rupture is induced by actin-based nucleus confinement. *J. Cell Biol.* 215:27–36. <https://doi.org/10.1083/jcb.201603053>
- Hung, W.C., J.R. Yang, C.L. Yankaskas, B.S. Wong, P.H. Wu, C. Pardo-Pastor, S.A. Serra, M.J. Chiang, Z. Gu, D. Wirtz, et al. 2016. Confinement Sensing and Signal Optimization via Piezo1/PKA and Myosin II Pathways. *Cell Reports.* 15:1430–1441. <https://doi.org/10.1016/j.celrep.2016.04.035>
- Irianto, J., C.R. Pfeifer, R.R. Bennett, Y. Xia, I.L. Ivanovska, A.J. Liu, R.A. Greenberg, and D.E. Discher. 2016. Nuclear constriction segregates mobile nuclear proteins away from chromatin. *Mol. Biol. Cell.* 27: 4011–4020. <https://doi.org/10.1091/mbc.E16-06-0428>
- Irianto, J., Y. Xia, C.R. Pfeifer, A. Athirasala, J. Ji, C. Alvey, M. Tewari, R.R. Bennett, S.M. Harding, A.J. Liu, et al. 2017. DNA Damage Follows Repair Factor Depletion and Portends Genome Variation in Cancer Cells after Pore Migration. *Curr. Biol.* 27:210–223. <https://doi.org/10.1016/j.cub.2016.11.049>
- Kanellos, G., J. Zhou, H. Patel, R.A. Ridgway, D. Huels, C.B. Gurniak, E. Sandilands, N.O. Carragher, O.J. Sansom, W. Witke, et al. 2015. ADF and Cofilin Control Actin Stress Fibers, Nuclear Integrity, and Cell Survival. *Cell Reports.* 13:1949–1964. <https://doi.org/10.1016/j.celrep.2015.10.056>
- Khatau, S.B., C.M. Hale, P.J. Stewart-Hutchinson, M.S. Patel, C.L. Stewart, P.C. Searson, D. Hodzic, and D. Wirtz. 2009. A perinuclear actin cap regulates nuclear shape. *Proc. Natl. Acad. Sci. USA.* 106:19017–19022. <https://doi.org/10.1073/pnas.0908686106>
- Kudo, N., N. Matsumori, H. Taoka, D. Fujiwara, E.P. Schreiner, B. Wolff, M. Yoshida, and S. Horinouchi. 1999. Leptomycin B inactivates CRM1/exportin 1 by covalent modification at a cysteine residue in the central conserved region. *Proc. Natl. Acad. Sci. USA.* 96:9112–9117. <https://doi.org/10.1073/pnas.96.16.9112>

- Kundu, P.K., I.M. Cohen, and D.R. Dowling. 2011. *Fluid Mechanics*. Academic Press, Waltham, MA. 318 pp.
- Lammerding, J. 2011. Mechanics of the nucleus. *Compr. Physiol.* 1:783–807.
- Le Berre, M., J. Aubertin, and M. Piel. 2012. Fine control of nuclear confinement identifies a threshold deformation leading to lamina rupture and induction of specific genes. *Integr. Biol.* 4:1406–1414. <https://doi.org/10.1039/c2ib20056b>
- Lombardi, M.L., D.E. Jaalouk, C.M. Shanahan, B. Burke, K.J. Roux, and J. Lammerding. 2011. The interaction between nesprins and sun proteins at the nuclear envelope is critical for force transmission between the nucleus and cytoskeleton. *J. Biol. Chem.* 286:26743–26753. <https://doi.org/10.1074/jbc.M111.233700>
- McGregor, A.L., C.R. Hsia, and J. Lammerding. 2016. Squish and squeeze—the nucleus as a physical barrier during migration in confined environments. *Curr. Opin. Cell Biol.* 40:32–40. <https://doi.org/10.1016/j.ceb.2016.01.011>
- Meijering, E., O. Dzyubachyk, and I. Smal. 2012. Methods for cell and particle tracking. *Methods Enzymol.* 504:183–200. <https://doi.org/10.1016/B978-0-12-391857-4.00009-4>
- Pajewski, J.D., K.N. Dahl, F.L. Zhong, P.J. Sannak, and D.E. Discher. 2007. Physical plasticity of the nucleus in stem cell differentiation. *Proc. Natl. Acad. Sci. USA.* 104:15619–15624. <https://doi.org/10.1073/pnas.0702576104>
- Paul, C.D., D.J. Shea, M.R. Mahoney, A. Chai, V. Laney, W.C. Hung, and K. Konstantopoulos. 2016. Interplay of the physical microenvironment, contact guidance, and intracellular signaling in cell decision making. *FASEB J.* 30:2161–2170. <https://doi.org/10.1096/fj.201500199R>
- Paul, C.D., P. Mistriotis, and K. Konstantopoulos. 2017. Cancer cell motility: lessons from migration in confined spaces. *Nat. Rev. Cancer.* 17:131–140. <https://doi.org/10.1038/nrc.2016.123>
- Petrie, R.J., and K.M. Yamada. 2016. Multiple mechanisms of 3D migration: the origins of plasticity. *Curr. Opin. Cell Biol.* 42:7–12. <https://doi.org/10.1016/j.ceb.2016.03.025>
- Petrie, R.J., H. Koo, and K.M. Yamada. 2014. Generation of compartmentalized pressure by a nuclear piston governs cell motility in a 3D matrix. *Science.* 345:1062–1065. <https://doi.org/10.1126/science.1256965>
- Raab, M., M. Gentili, H. de Belly, H.R. Thiam, P. Vargus, A.J. Jimenez, F. Lautenschlaeger, R. Voituriez, A.M. Lennon-Duménil, N. Manel, and M. Piel. 2016. ESCRT III repairs nuclear envelope ruptures during cell migration to limit DNA damage and cell death. *Science.* 352:359–362. <https://doi.org/10.1126/science.aad7611>
- Rajanala, K., and V.K. Nandicoori. 2012. Localization of nucleoporin Tpr to the nuclear pore complex is essential for Tpr mediated regulation of the export of unspliced RNA. *PLoS One.* 7:e29921. <https://doi.org/10.1371/journal.pone.0029921>
- Rowat, A.C., D.E. Jaalouk, M. Zwerger, W.L. Ung, I.A. Eydelnant, D.E. Olins, A.L. Olins, H. Herrmann, D.A. Weitz, and J. Lammerding. 2013. Nuclear envelope composition determines the ability of neutrophil-type cells to passage through micron-scale constrictions. *J. Biol. Chem.* 288: 8610–8618. <https://doi.org/10.1074/jbc.M112.441535>
- Sahai, E., and C.J. Marshall. 2003. Differing modes of tumour cell invasion have distinct requirements for Rho/ROCK signalling and extracellular proteolysis. *Nat. Cell Biol.* 5:711–719. <https://doi.org/10.1038/ncb1019>
- Sao, K., T.M. Jones, A.D. Doyle, D. Maity, G. Schevzov, Y. Chen, P.W. Gunning, and R.J. Petrie. 2019. Myosin II governs intracellular pressure and traction by distinct tropomyosin-dependent mechanisms. *Mol. Biol. Cell.* 30:1170–1181. <https://doi.org/10.1091/mbc.E18-06-0355>
- Snow, C.J., A. Dar, A. Dutta, R.H. Kehlenbach, and B.M. Paschal. 2013. Defective nuclear import of Tpr in Progeria reflects the Ran sensitivity of large cargo transport. *J. Cell Biol.* 201:541–557. <https://doi.org/10.1083/jcb.201212117>
- Stelma, T., A. Chi, P.J. van der Watt, A. Verrico, P. Lavia, and V.D. Leaner. 2016. Targeting nuclear transporters in cancer: Diagnostic, prognostic and therapeutic potential. *IUBMB Life.* 68:268–280. <https://doi.org/10.1002/iub.1484>
- Stewart, M. 2007. Molecular mechanism of the nuclear protein import cycle. *Nat. Rev. Mol. Cell Biol.* 8:195–208. <https://doi.org/10.1038/nrm2114>
- Stewart-Hutchinson, P.J., C.M. Hale, D. Wirtz, and D. Hodzic. 2008. Structural requirements for the assembly of LINC complexes and their function in cellular mechanical stiffness. *Exp. Cell Res.* 314:1892–1905. <https://doi.org/10.1016/j.yexcr.2008.02.022>
- Stroka, K.M., H. Jiang, S.H. Chen, Z. Tong, D. Wirtz, S.X. Sun, and K. Konstantopoulos. 2014. Water permeation drives tumor cell migration in confined microenvironments. *Cell.* 157:611–623. <https://doi.org/10.1016/j.cell.2014.02.052>
- Takaki, T., M. Montagner, M.P. Serres, M. Le Berre, M. Russell, L. Collinson, K. Szuhai, M. Howell, S.J. Boulton, E. Sahai, and M. Petronczki. 2017. Actomyosin drives cancer cell nuclear dysmorphia and threatens genome stability. *Nat. Commun.* 8:16013. <https://doi.org/10.1038/ncomms16013>
- Thomas, D.G., A. Yeneppalli, C.M. Denais, A. Rape, J.R. Beach, Y.L. Wang, W.P. Schiemann, H. Baskaran, J. Lammerding, and T.T. Egelhoff. 2015. Non-muscle myosin IIB is critical for nuclear translocation during 3D invasion. *J. Cell Biol.* 210:583–594. <https://doi.org/10.1083/jcb.201502039>
- Tinevez, J.Y., U. Schulze, G. Salbreux, J. Roensch, J.F. Joanny, and E. Paluch. 2009. Role of cortical tension in bleb growth. *Proc. Natl. Acad. Sci. USA.* 106:18581–18586. <https://doi.org/10.1073/pnas.0903353106>
- van Helvert, S., C. Storm, and P. Friedl. 2018. Mechanoreciprocity in cell migration. *Nat. Cell Biol.* 20:8–20. <https://doi.org/10.1038/s41556-017-0012-0>
- Vartiainen, M.K., S. Guettler, B. Larijani, and R. Treisman. 2007. Nuclear actin regulates dynamic subcellular localization and activity of the SRF cofactor MAL. *Science.* 316:1749–1752. <https://doi.org/10.1126/science.1141084>
- Wang, P., F. Zhu, and K. Konstantopoulos. 2012. The antagonistic actions of endogenous interleukin-1 $\beta$  and 15-deoxy- $\Delta$ 12,14-prostaglandin J2 regulate the temporal synthesis of matrix metalloproteinase-9 in sheared chondrocytes. *J. Biol. Chem.* 287:31877–31893. <https://doi.org/10.1074/jbc.M112.362731>
- Weigel, B., G.J. Bakker, and P. Friedl. 2012. Intravital third harmonic generation microscopy of collective melanoma cell invasion: Principles of interface guidance and microvesicle dynamics. *Intravital.* 1:32–43. <https://doi.org/10.4161/intv.21223>
- Wiggin, O., B. Schroder, D. Krapf, J.R. Bamburg, and J.G. DeLuca. 2017. Cofilin Regulates Nuclear Architecture through a Myosin-II Dependent Mechanotransduction Module. *Sci Rep-Uk.* 7. <https://doi.org/10.1038/srep40953>
- Wolf, K., M. Te Lindert, M. Krause, S. Alexander, J. Te Riet, A.L. Willis, R.M. Hoffman, C.G. Figdor, S.J. Weiss, and P. Friedl. 2013. Physical limits of cell migration: control by ECM space and nuclear deformation and tuning by proteolysis and traction force. *J. Cell Biol.* 201:1069–1084. <https://doi.org/10.1083/jcb.201210152>
- Wolff, B., J.J. Sanglier, and Y. Wang. 1997. Leptomycin B is an inhibitor of nuclear export: inhibition of nucleocytoplasmic translocation of the human immunodeficiency virus type 1 (HIV-1) Rev protein and Rev-dependent mRNA. *Chem. Biol.* 4:139–147. [https://doi.org/10.1016/S1074-5521\(97\)90257-X](https://doi.org/10.1016/S1074-5521(97)90257-X)
- Xia, Y., I.L. Ivanovska, K. Zhu, L. Smith, J. Irianto, C.R. Pfeifer, C.M. Alvey, J. Ji, D. Liu, S. Cho, et al. 2018. Nuclear rupture at sites of high curvature compromises retention of DNA repair factors. *J. Cell Biol.* 217:3796–3808. <https://doi.org/10.1083/jcb.201711161>